

LoCo: Low-Bit Communication Adaptor for Large-scale Model Training

Xingyu Xie, Zhijie Lin, Kim-Chuan Toh, Pan Zhou

Abstract—To efficiently train large-scale models, low-bit gradient communication compresses full-precision gradients on local GPU nodes into low-precision ones for higher gradient synchronization efficiency among GPU nodes. However, it often degrades training quality due to compression information loss. To address this, we propose the Low-bit Communication Adaptor (LoCo), which compensates gradients on local GPU nodes before compression, ensuring efficient synchronization without compromising training quality. Specifically, LoCo designs a moving average of historical compensation errors to stably estimate concurrent compression error and then adopts it to compensate for the concurrent gradient compression, yielding a less lossless compression. This mechanism allows it to be compatible with general optimizers like Adam and sharding strategies like FSDP. Theoretical analysis shows that integrating LoCo into full-precision optimizers like Adam and SGD does not impair their convergence speed on nonconvex problems. Experimental results show that across large-scale model training frameworks like Megatron-LM and PyTorch’s FSDP, LoCo significantly improves communication efficiency, e.g., improving Adam’s training speed by 14% to 40% without performance degradation on large language models like LLAMAs and MoE.

Index Terms—Efficient Large-Scale Training, Large-Scale Optimization, Deep Learning Optimization



1 INTRODUCTION

DEEP learning has made remarkable strides across various domains in recent decades, such as language modeling [1], [2], computer vision [3], and multi-modality [4]. This progress is largely attributed to the advent of large-scale models, like the GPT and LLAMA series [1], [5]–[7], characterized by their billions of parameters and trillions of training tokens. This trend of large-scale models has expanded into various other fields, including finance [8], law [9], and medicine [10]. Despite their successes, these large-scale models necessitate extensive GPUs for parallel training, employing strategies like data parallelism [11], pipeline parallelism [12], tensor parallelism [13]. A major challenge in this parallel training is the frequent gradient communication for synchronization among GPUs, which significantly burdens the communication system. In fact, the communication time can even consume over 50% of the total training time in some cases [14], [15].

To relieve the communication burden, one often adopts compression techniques, e.g., quantization, to compress the full-precision communication variables into low-precision formats, e.g., 32-bit gradient to 8-bit one. While significantly improving communication efficiency among GPU nodes, this compression often brings substantial challenges in maintaining training quality due to information loss. Notably, low-bit gradients (e.g., less than 8-bit) are not typically supported by hardware, and their computations, e.g., addition, often suffer from overflow. Consequently, advanced frameworks like Megatron-LM [13] and Pytorch Fully Sharded Data Parallelism (FSDP) [16], though capable of low-bit computations

for weights and activations, still need high-precision gradient for communication to avoid performance degradation that is particularly pronounced in models like LLMs. This well testifies the significant challenges in gradient compression for training large-scale models.

To address the challenge of communication efficiency in large-scale model training, error-feedback compression [17], [18] (EFC) has been developed to compensate for communication variables before compression, ensuring small compression errors. This technique has been utilized in gradient compression to create communication-efficient low-bit optimizers, such as 1-bit Adam [14] and 1-bit LAMB [19]. However, these low-bit optimizers face several key challenges. Firstly, most EFC methods [18], [20], [21] are designed for master-server communication system (MSC) and cannot be directly applied to ring- and tree-based communication systems (RC and TC), which significantly enhance MSC efficiency [22] and are the default settings for current LLM training. Secondly, EFC-based optimizers, such as 1-bit Adam, often require maintaining a global error variable (equivalent to the model size), that is stored and communicated among GPU nodes in MSC. This introduces substantial additional communication and memory overheads, which are unaffordable for LLM training. Finally, in the context of FSDP, where model parameters and optimizer states are partitioned and distributed across multiple devices, EFC-based methods face additional challenges. For example, optimizers such as 1-bit Adam and 1-bit LAMB, which rely on compressing and communicating optimizer states, become less effective because FSDP does not maintain or communicate complete optimizer states during backpropagation. This complicates the updating of optimizer states without incurring additional overhead. Additionally, methods that require full parameters for subsequent computation, e.g., computing specific statistics in IntSGD [23], introduce extra communication costs in FSDP settings. See Sec. 2 for more details on MSC, RC, and modern sharding strategy.

- X. Xie and K.C. Toh are with the Department of Mathematics, National University of Singapore, Singapore.
- P. Zhou is with the School of Computing and Information Systems, Singapore Management University, Singapore. Email: panzhou@smu.edu.sg.
- P. Zhou and Z. Lin were previously with Sea AI Lab, Singapore.

Contribution. In this work, we design an effective gradient compression approach to improve the communication efficiency of widely used optimizers like Adam and AdamW, particularly in RC, TC, and FSDP settings. We introduce the novel Low-bit Communication Adaptor (LoCo) that can compress full-precision gradients into low-precision ones with small information loss, enhancing communication efficiency in large-model training. The key to LoCo is a refined error-feedback mechanism: it estimates more stable compression errors using a moving average of historical errors and strategically incorporates these errors back into the gradient before compression to reduce compression error. This strategy decouples LoCo from specific optimization algorithms, making it compatible with various optimizers, such as Adam [24] and AdaFactor [25], and integrates seamlessly with modern sharding strategies like FSDP, RC, and TC. Furthermore, LoCo has been adapted to popular large-scale model training frameworks such as Megatron-LM and PyTorch’s FSDP. This compatibility ensures that LoCo can be effectively employed in diverse large-model training environments, providing robust support for scaling up training processes.

An important aspect of our work is the theoretical analysis, demonstrating that for nonconvex problems—including the training of large-scale models—integrating LoCo with standard optimizers like SGD and Adam-type algorithms does not adversely affect their convergence speed. This ensures that these optimizers retain their effectiveness even when operating with low-precision gradients.

Extensive experiments show that LoCo significantly improves efficiency while maintaining performance comparable to full-precision optimizers. For instance, on various large language models, such as LLAMAs and MoE-Mixtral [26] with model sizes ranging from 7B to 70B parameters, LoCo enhances the overall training speed of Adam by 14% to 40% while preserving comparable downstream task performance as Adam with full-precision gradients. This demonstrates the effectiveness of LoCo in alleviating communication burdens in large-model training.

2 PRELIMINARY AND RELATED WORK

2.1 Communication among GPU Nodes

The Master-Server communication pattern is a structure where a single “master” node exercises control over multiple server nodes. In this setup, all communication flows from the master to the servers. However, this centralization means that the master node can become a bottleneck, leading to potential congestion and delays in communication, particularly when the master node is handling a high volume of requests. Additionally, this architecture can suffer from a single point of failure: if the master node fails, it can have a disastrous impact on the entire system.

On the other hand, the Ring-based communication method is a decentralized approach where each node in the cluster is connected in a ring formation. This structure allows for high levels of parallelism, as each node can simultaneously send and receive information to and from its immediate neighbors. The RC method can efficiently distribute the load across all nodes, avoiding the bottleneck issue seen in master-server communication [22]. However, one of the challenges

of this approach is that it may require multiple rounds of communication to disseminate information throughout the entire ring, as each node only communicates with its immediate neighbors.

2.2 Fully Sharded Data Parallelism

FSDP has emerged as the preferred training method for large-scale machine learning models, addressing limitations that make Distributed Data Parallel (DDP) unsuitable for such tasks. DDP, which requires each GPU to maintain a full replica of the model, faces significant memory constraints when dealing with models that have billions of parameters. In contrast, FSDP improves scalability by sharding model parameters, gradients, and optimizer states across multiple devices. This sharding process allows FSDP to dynamically gather only the necessary shards for computation, thus substantially reducing memory usage and enabling efficient training of extremely large models. Integrated into frameworks like PyTorch and Megatron-LM [13], [27], FSDP has shown considerable improvements in training speed and memory efficiency, solidifying its role as the default solution for large model training [16], [28]. For a comprehensive background and discussion, please refer to Appendix Sec. A.2.

2.3 Communication-efficient Training

Recently, AI models have become much larger than before, like billion-scale language models and multi-modal models [6], [26], and their training bottleneck is often the high communication cost caused by the very high-dimensional gradient communication among GPUs. To alleviate this issue, one often compresses the gradient before its communication. Currently, compression techniques mainly contain gradient quantization [17], [29], [30], gradient sparsification [31]–[33], and decentralization [34], [35]. Among them, gradient quantization aims to quantize the high precision gradient into a low-bit one for reducing communication cost, and has shown promising efficiency for model training, e.g., 1-bit Adam [14] and 0/1 Adam [15] of which both compress the entries in the gradient-based statistics into ± 1 .

2.4 Error-feedback Compression

Gradient compression often introduces information loss, leading to accumulated errors that can cause algorithmic divergence. To address this, Seide et al. [17] proposed the first error-feedback compression (EFC) strategy, which compensates for compression errors by adding them back into the gradient before compression. This method demonstrated effectiveness in 1-bit SGD. After this, EF21 was proposed [18], a theoretically and practically improved EFC variant, which has inspired further theoretical developments [21], [36]–[38]. Practical adaptations of EFC have also been explored, incorporating gradient quantization into adaptive gradient algorithms to develop communication-efficient variants, such as 1-bit Adam [14] and 0/1 Adam [15]. Adaptive gradient algorithms like AdaGrad [39], Adam [24], and Adan [40] adjust learning rates for each gradient coordinate based on the curvature of the training loss, offering faster convergence than SGD. Combining EFC with these adaptive algorithms enhances training efficiency while maintaining comparable performance to their uncompressed counterparts.

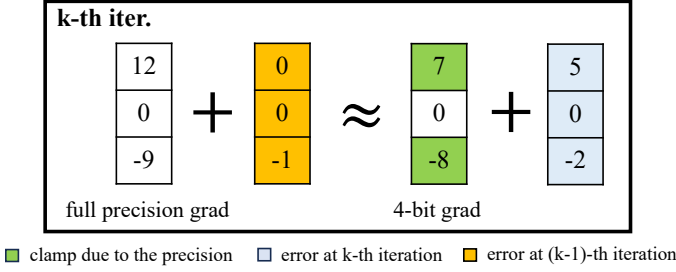


Fig. 1: Illustration of LoCo. At iteration k , before compression, LoCo compensates the full-precision gradient with the compression error from previous iterations to reduce the compression error. Then, it compresses the gradient into a low-bit one for fast communication among GPU nodes.

Despite the promising results of EFC, most implementations are tailored for the master-server communication pattern, limiting their applicability in FSDP. Some EFC-based methods, such as PowerSGD [41], can train neural networks with DDP patterns, but they encounter challenges in the FSDP setting. For instance, in PyTorch’s FSDP framework, gradients retrieved in the communication hook are flattened, complicating the application of matrix decomposition-based compression techniques like PowerSGD, which rely on the original gradient shapes.

2.5 Challenges in Migrating EFC to FSDP

Migrating EFC methods from MSC to RC or TC frameworks necessitates addressing significant challenges associated with maintaining the global error variable. In the original EFC algorithms, a global error variable compensates for compression errors. Removing this global variable is crucial to reduce memory and communication overheads, as maintaining a copy of the global error variable on each node would be inefficient.

Sharding Conflict: Specifically, for optimizers like 1-bit Adam and 0/1 Adam, which use optimizer state communication instead of gradient communication, transitioning to FSDP is particularly challenging. In the FSDP context, gradients are complete during the backward pass and can be effectively reduced and scattered. However, using optimizer states for model updates requires additional communication of these states, leading to increased overhead that contradicts the sharding strategy’s goal of minimizing communication.

Memory Constraints with Optimizer States: Some methods, such as 0/1 Adam and EF21-SGD2M [42], compress or communicate optimizer states, leading to significant memory management challenges. While gradients can be discarded after communication to free up memory, optimizer states, particularly first-order moments, must be retained for subsequent update iterations. These persistent states impose significant memory demands in sharded environments. Furthermore, optimizer states are not suitable for low-precision representation. For instance, FP8-LM [43] demonstrates that the precision of optimizer states significantly impacts model training quality. Detailed experiments from FP8-LM show that optimizer states require precision higher than 16-bit for effective training. In contrast, our LoCo maintains only a local average of the compressed errors, which is less sensitive to precision and can be stored in 8-bit format without impacting training effectiveness.

Algorithm 1: LoCo (Low-bit Communication Adaptor)

Input: initialization θ_0 , compression scalar s and s_e , reset frequency T_c , $\beta \in [0, 1]$.
Output: model weight θ_K at the K -th iteration.

- 1 **while** $k < K$ **do**
- 2 **Step 1. Low-Bit Gradient Estimation**
- 3 | estimate the gradient \mathbf{g}_k^n at θ_k on Node n ;
- 4 | $\mathbf{h}_{k+1}^n = \mathbf{g}_k^n + \text{decompressor}(\mathbf{e}_k^n; s_e)$;
- 5 | $\tilde{\mathbf{h}}_{k+1}^n = \text{compressor}(\mathbf{h}_{k+1}^n; s, 4)$;
- 6 **Step 2. Compensation Error Estimation**
- 7 | $\mathbf{d}_{k+1}^n = \text{decompressor}(\tilde{\mathbf{h}}_{k+1}^n; s)$;
- 8 | $\tilde{\mathbf{e}}_{k+1}^n = (1 - \beta)\tilde{\mathbf{e}}_k^n + \beta(\mathbf{h}_{k+1}^n - \mathbf{d}_{k+1}^n)$;
- 9 | **if** $k \% T_c = 0$ **then**
- 10 | | $\mathbf{e}_{k+1}^n = \mathbf{0}$; // error reset
- 11 | **else**
- 12 | | $\mathbf{e}_{k+1}^n = \text{compressor}(\tilde{\mathbf{e}}_{k+1}^n; s_e, 8)$;
- 13 | **end if**
- 14 **Step 3. Communication and Model Update**
- 15 | $\tilde{\mathbf{g}}_k = \frac{1}{N} \sum_{n=1}^N \text{decompressor}(\tilde{\mathbf{h}}_{k+1}^n)$;
- 16 | use $\tilde{\mathbf{g}}_k$ to update θ_k on Node n ;
- 17 **end while**

Matrix Decomposition Compression Challenges: Additionally, methods based on matrix decomposition, such as PowerSGD [41], face difficulties in the FSDP context. In PyTorch’s FSDP framework, gradients retrieved in the communication hook are flattened, complicating the application of matrix decomposition techniques that rely on the gradients’ original shapes. This restriction prevents the straightforward application of such compression methods, further highlighting the challenges of adapting EFC to FSDP.

3 LOW-BIT COMMUNICATION ADAPTOR

To address the communication burden in large-model training on many GPU nodes, we introduce an efficient and novel low-bit communication adapter, LoCo. As shown in Fig. 1, the core idea of LoCo is to quantize the full-precision gradient into a lower-precision one with error-feedback for improving communication efficiency, e.g., compressing a 32-bit gradient into a 4-bit one. A critical challenge in gradient compression is that its compression error accumulates along training iterations and can lead to failure in model training. To solve this issue, LoCo employs a novel error-feedback compression strategy in Algorithm 1 to reduce accumulated errors and ensure high-quality compression. The strategy encompasses three key steps: 1) low-bit gradient estimation, 2) compensation error estimation, and 3) gradient communication and model update. Initially, LoCo computes the stochastic gradient on each GPU and compensates it before compression to a low-bit format. The compensation error estimation step integrates the current and historical compensation errors to mitigate gradient compression error accumulation in subsequent steps. The final step involves aggregating the average of low-bit gradients across GPUs, which is subsequently followed by the model update using optimizers like Adam and Adafactor. Detailed elaboration on these steps will be provided below.

3.1 Low-bit Gradient Estimation

As shown in Algorithm 1, for parallel training with N GPU nodes, each node receives a minibatch of data at each iteration to compute the minibatch stochastic gradient \mathbf{g}_k^n . The key challenge is to compress the high-precision gradient \mathbf{g}_k^n into a low-precision form without causing significant accumulated compression errors in each iteration. This ensures that low-bit gradients can be efficiently transferred among GPUs while maintaining the training quality.

Accordingly, we design an efficient and effective error-feedback-based compression strategy. Specifically, we first define the element-wise compression operation and its inverse operation as follows:

$$\begin{cases} \text{compressor}(\mathbf{h}; s, p) := \text{round}_{p\text{-bit}}(\mathbf{h} \times s), \\ \text{decompressor}(\tilde{\mathbf{h}}; s) := \text{float}(\tilde{\mathbf{h}})/s, \end{cases} \quad (1)$$

where $s > 0$ denotes a hyper-parameter that modulates the low-bit scale, and the rounding function $\text{Round}_{p\text{-bit}}$ is defined to round each floating-point number to its nearest integer within the range of -2^{p-1} to $2^{p-1} - 1$, such as -8 to $+7$ in $\text{Round}_{4\text{-bit}}$ operation. The operation in Eqn. (1) is a commonly used quantization method. While more advanced methods like IntSGD [23] exist, we found that the default one in PyTorch, Eqn. (1), is sufficient for our tasks.

Given the current compensation error \mathbf{e}_k^n , we first add it back to the current stochastic gradient \mathbf{g}_k^n on each node:

$$\mathbf{h}_{k+1}^n = \mathbf{g}_k^n + \text{decompressor}(\mathbf{e}_k^n; s_e). \quad (2)$$

In LoCo, to save memory on each GPU, we use an 8-bit compensation error \mathbf{e}_k^n which is quantized by the operation $\text{compressor}(\mathbf{h}; s_e, 8)$ with scale s_e in Eqn. (1). Here $\text{decompressor}(\mathbf{e}_k^n; s_e)$ inversely transfers 8-bit \mathbf{e}_k^n into its float version for addition with \mathbf{g}_k^n . In Sec. 3.2, we will introduce the compensation error $\tilde{\mathbf{e}}_k^n$ which intuitively denotes the average of the previous gradient compression error.

Next, on each node, we compress the high-precision compensated gradient $\tilde{\mathbf{h}}_{k+1}^n$ into its low-bit version:

$$\tilde{\mathbf{h}}_{k+1}^n = \text{compressor}(\mathbf{h}_{k+1}^n; s, 4). \quad (3)$$

In our experiments, we set a scaling factor $s = 2^{19}$ for fine-tuning and $s \in \{2^{19}, 2^{17}\}$ for pre-training. In practice, we find that 4-bit can balance communication efficiency and performance well. Indeed, Fig. 2 shows that 4-bit LoCo can achieve comparable training loss as 16-bit based Adam.

Finally, one can transfer the low-bit compensated gradient $\tilde{\mathbf{h}}_{k+1}^n$ among GPU nodes to compute their average for the model update by using an optimizer. See details in Sec. 3.3. Compared to 32-bit gradients, using 4-bit gradients for communication significantly enhances communication efficiency, particularly in environments with numerous GPUs. As the number of GPUs or the model size increases, communication costs grow linearly. This increase in communication overhead can cause GPUs to idle, waiting for data transfer, leading to a notable degradation in overall computational efficiency.

3.2 Compensation Error Estimation

Compression inherently leads to information loss, which is a significant challenge in gradient compression. Our approach focuses on estimating a compensation error $\tilde{\mathbf{e}}_k^n$ to mitigate

error accumulation. The 8-bit compensation error \mathbf{e}_k^n used in Eqn. (2) is a memory-efficient, compressed version of $\tilde{\mathbf{e}}_k^n$ to conserve GPU memory. A straightforward solution is to set the compensation error as the gradient compression error from the previous iteration, as implemented in the EFC [17]:

$$\tilde{\mathbf{e}}_k^n = \underset{\mathbf{e}}{\text{argmin}} \|\mathbf{e} + \mathbf{d}_k^n - \mathbf{h}_k^n\|^2 = \mathbf{h}_k^n - \mathbf{d}_k^n, \quad (4)$$

where $\mathbf{d}_k^n = \text{decompressor}(\tilde{\mathbf{h}}_k^n; s)$ decompresses the low-bit compensated gradient $\tilde{\mathbf{h}}_k^n$ into high-precision floating number for computation, and $\|\cdot\|$ is the vector ℓ_2 norm.

Unfortunately, we empirically find that this estimation is not stable. This is because compression operations, e.g., our rounding operation, top-k operation [44] and random sparsification [45], often inherently exhibit discontinuous properties, and bring abrupt fluctuations in compensation error. This means that $\tilde{\mathbf{e}}_k^n$ suffers from large variance. As a result, using $\tilde{\mathbf{e}}_k^n$ to compensate the gradient in Eqn. (3) would also bring abrupt fluctuations into the low-bit gradient, potentially failing the model training. To relieve this issue, we regularize the current compensation error $\tilde{\mathbf{e}}_k^n$ to be not too far from the previous one $\tilde{\mathbf{e}}_{k-1}^n$. This can avoid big $\tilde{\mathbf{e}}_k^n$ fluctuations and improve its smoothness. Formally, we have:

$$\begin{aligned} \tilde{\mathbf{e}}_k^n &= \underset{\mathbf{e}}{\text{argmin}} \frac{\beta}{2} \|\mathbf{e} + \mathbf{d}_k^n - \mathbf{h}_k^n\|^2 + \frac{1-\beta}{2} \|\mathbf{e} - \tilde{\mathbf{e}}_{k-1}^n\|^2 \\ &= (1-\beta)\tilde{\mathbf{e}}_{k-1}^n + \beta(\mathbf{h}_k^n - \mathbf{d}_k^n), \end{aligned} \quad (5)$$

where $0 \leq \beta \leq 1$ is a parameter to balance the two terms, and $\tilde{\mathbf{e}}_0^n$ is initialized as zero. One can observe that Eqn. (5) effectively averages all historical compression errors to estimate the compensation error, thus avoiding large fluctuations better than Eqn. (4). Some EFC-based methods, like EF21-SGD2M [42], suggest that moving averages may have theoretical benefits. However, they apply the average to the gradient rather than the error, resembling a combination of EFC and adaptive optimizers rather than addressing the instability issues targeted by our method.

Moreover, when using SGD or Adam-type optimizers to update the model, the model weight at the k -th iteration can be formulated as $\boldsymbol{\theta}_k = \boldsymbol{\theta}_0 - \sum_{i=1}^k \boldsymbol{\eta}_i \circ \mathbf{g}_i$, where \mathbf{g}_i is the high-precision gradient. For SGD, its element-wise learning rate $\boldsymbol{\eta}_i$ is a constant $\boldsymbol{\eta}$, while for Adam-type optimizers, e.g., Adam, it is the combination of a preconditioner and a constant learning rate $\boldsymbol{\eta}$ (see Eqn. (9) in Sec. 4), and is also of the order $\mathcal{O}(\boldsymbol{\eta})$. In this context, for LoCo, we can show that:

$$\left\| \sum_{i=1}^k \boldsymbol{\eta}_i \circ \mathbf{g}_i - \sum_{i=1}^k \boldsymbol{\eta}_i \circ \tilde{\mathbf{g}}_i \right\| = \mathcal{O}(\boldsymbol{\eta} \|\tilde{\mathbf{e}}_k\|) = \mathcal{O}(\boldsymbol{\eta}), \quad (6)$$

where $\tilde{\mathbf{g}}_i$ is the low-precision counterpart of gradient \mathbf{g}_i . This indicates that although the compression error $\|\mathbf{g}_k - \tilde{\mathbf{g}}_k\|$ for a single iteration is of the order $\mathcal{O}(\|\tilde{\mathbf{e}}_k\|) = \mathcal{O}(\boldsymbol{\eta})$, the compression error over iterations will *not* accumulate and remains at the order of $\mathcal{O}(\boldsymbol{\eta})$. This is because the difference between the accumulated high-precision gradients $\sum_{i=1}^k \boldsymbol{\eta}_i \circ \mathbf{g}_i$ and low-precision gradients $\sum_{i=1}^k \boldsymbol{\eta}_i \circ \tilde{\mathbf{g}}_i$ does not increase with the number of iterations. This demonstrates LoCo's capability to mitigate error accumulation. For a formal illustration and analysis, please refer to Lemma 3 in Appendix 4.

To save GPU memory footprint, we further compress the high-precision compensation error $\tilde{\mathbf{e}}_k^n$ into an 8-bit version

e_k^n on each node. This is important and necessary for large-model training settings since compensation error is of the same size as the model and brings GPU memory overhead.

Moreover, we periodically reset the compensation error. This is because, along with training iterations, the compensation errors in the early iterations are out of date and are not suitable for current compensation error estimation due to the ever-changing optimization process and landscape. This is especially true for network training due to their fast-changing landscape during optimization. In this way, we arrive at our final low-bit compensation error e_k^n :

$$e_{k+1}^n = \begin{cases} \mathbf{0}, & \text{if } k \% T_c = 0, \\ \text{compressor}(\tilde{e}_{k+1}^n; s_e, 8), & \text{otherwise.} \end{cases} \quad (7)$$

We set $T_c \in \{512, 1024\}$ for all experiments, which works well, and set $s_e = 4s$ or $6s$ where s is used in Eqn. (3). In practice, on large-model training, e.g., LLAMA, with this 8-bit quantization, LoCo improves the token throughput by 10% – 40%+ while only bringing a marginal memory overhead of less than 10%. See results in Tables 7 and 8.

3.3 Communication and Model Update

To synchronize the gradients for model update at the k -th iteration, we need to collect low-bit gradients $\{\tilde{\mathbf{h}}_{k+1}^n\}_{n=1}^N$ from all N GPU nodes, and compute their average

$$\tilde{\mathbf{g}}_k = \frac{1}{N} \sum_{n=1}^N \text{decompressor}(\tilde{\mathbf{h}}_{k+1}^n), \quad (8)$$

where $\text{decompressor}(\cdot)$ decompresses the 4-bit gradient $\tilde{\mathbf{h}}_{k+1}^n$ into high-precision floating number, which is then used in the optimizer for the model update on each node.

Considering the demands of large-scale model training, we adopt the FSDP strategy that is commonly used for training LLMs [13], [28]. FSDP partitions the d -dimensional gradient into N blocks, e.g., $\tilde{\mathbf{h}}_k^n := [\tilde{\mathbf{h}}_{k,1}^n, \dots, \tilde{\mathbf{h}}_{k,N}^n]$ on the n -th node. Then each node only collects its corresponding portion from all other nodes, e.g., $\frac{1}{N} \sum_{i=1}^N \text{decompressor}(\mathbf{h}_{k,n}^i)$ on the n -th node, to save memory and communication cost.

Under RC and TC settings, which are widely used for training large-scale models, gradient averaging typically employs the reduce-scatter operation. However, to collect gradients on all GPU nodes, reduce-scatter requires each node to decompress, sum, and recompress the low-bit vectors. This complex process progressively increases information loss due to numerical anomalies such as overflow or underflow. To address this issue, we adopt the all-to-all (all2all) strategy. In the all2all approach, the n -th node first gathers all low-bit gradient partitions $[\mathbf{h}_{k,n}^1, \dots, \mathbf{h}_{k,n}^N]$, and then averages them in high precision locally. This method eliminates the intermediate steps in reduce-scatter, thus preventing information loss. Furthermore, all2all maintains computational and communication efficiency comparable to reduce-scatter. Consequently, we use all2all under RC and TC settings. For more details about all2all, see Appendix A.1.

3.4 Discussion and Comparison

Compared with previous communication-efficient network training algorithms like Zero++ [46], 1-bit Adam [14], 1-bit LAMB [19] and 0/1 Adam [15], LoCo distinguishes itself

from them through its low computational and memory demands, enabling effective low-bit gradient training in large-scale models. It incorporates algorithmic improvements that significantly reduce compression error accumulation over training iterations, advancing beyond methods that use compression without error-feedback, such as Zero++ [46]. A key advantage of LoCo is its high compatibility with various optimizers (e.g., Adam, AdaFactor), different communication settings (e.g., MSC, RC, and TC), and other components essential for large-model training, such as FSDP. This compatibility is achieved by decoupling its error-feedback strategy from these specific configurations. In contrast, other low-bit optimizers, such as 1-bit Adam, 1-bit LAMB, and 0/1 Adam, have error-feedback mechanisms specifically designed for MSC and certain optimizers, limiting their applicability to sharding strategies. This versatility aligns with the critical integration required for training SoTA LLMs and allows LoCo to be seamlessly integrated with more advanced techniques in the future.

4 CONVERGENCE GUARANTEE

In this section, we provide the convergence guarantee for the proposed LoCo when applied to two prevalent types of optimizers: SGD and Adam-family optimizers. We focus on the following nonconvex optimization problem:

$$\min_{\theta} f(\theta) := \mathbb{E}_{\zeta \sim \mathcal{D}}[F(\theta, \zeta)],$$

where $F(\cdot, \cdot)$ is differentiable and nonconvex, the data ζ is drawn from an unknown distribution \mathcal{D} , and θ is model weight. For analysis, we first make several mild assumptions.

Assumption 1 (*L-smoothness*). *The function $f(\cdot)$ is L -smooth w.r.t. the parameter, i.e., $\exists L > 0$, we have:*

$$\|\nabla f(\theta_1) - \nabla f(\theta_2)\|_2 \leq L \|\theta_1 - \theta_2\|_2, \quad \forall \theta_1, \theta_2.$$

Assumption 2 (*Boundedness*). *The gradient estimation \mathbf{g}_k on each GPU node is unbiased, i.e., $\mathbb{E}[\mathbf{g}_k] = \nabla f(\theta_k)$, and its magnitude and variance are bounded:*

$$\mathbb{E}\|\mathbf{g}_k\|_{\infty} \leq c_{\infty}, \quad \mathbb{E}\left[\|\nabla f(\theta_k) - \mathbf{g}_k\|_2^2\right] \leq \sigma^2.$$

Assumption 3 (*Bit-length*). *Support that the compression operations in (3) and (7) respectively use p -bit with a scalar s and p_e -bit with a scalar s_e . With the proper p , p_e , s , and s_e , there exist a constant $0 \leq \alpha < 1$ such that $(1 - \alpha)sc_{\infty} + s/2s_e \leq 2^p$ and $T_c\alpha\beta s_e c_{\infty} \leq 2^{p_e}$, where β is given in Eqn. (5).*

Assumptions 1 and 2 are mild and frequently used in the analysis of general nonconvex problems [47]–[50]. The bounded gradient assumption, while commonly utilized, is primarily necessary for the convergence analysis of Adam-family methods and is not specifically required by EFC. When considering only the SGD case, as with some EFC-based methods like EF21, LoCo’s convergence guarantee also holds without relying on the bounded gradient assumption. It is important to note that removing the bounded gradient assumption for the convergence analysis of Adam-family methods remains an open and challenging problem [51], [52]. We acknowledge this limitation and leave it for future work.

Assumption 3 quantifies the expected precision loss introduced by the two compression operations within Algorithm 1. 1) For the p -bit gradient compression operation,

we assume that in the worst-case scenario, the precision degradation does not exceed α times the upper bound of the gradient norm, denoted as αc_∞ , where $0 \leq \alpha < 1$. This is similar to the necessary condition $\|\tilde{\mathbf{e}}_{k+1}^n\|^2 \leq \alpha \|\mathbf{g}_k^n\|^2$ used in the analysis of biased SGD [53]. This assumption ensures that in extreme cases, the compression error does not surpass the gradient itself, thereby preserving a portion of the gradient information and preventing the complete loss of gradient direction; 2) For the p -bit error compression operation, which lacks a feedback mechanism, we assume that the precision degradation introduced by the error compression does not accumulate excessively during the error reset period. By appropriately setting hyper-parameters, such as in our practical choice of $p_e = 8$ and $p = 4$, this assumption ensures that the precision degradation from p_e -bit error compression remains less than that from p -bit gradient compression. This is a relatively weak condition and can be easily met.

Then, we investigate the convergence performance of LoCo-integrated SGD and Adam-type optimizers in turn.

4.1 LoCo-integrated SGD

For SGD, its algorithmic steps are as:

$$\text{SGD: } \boldsymbol{\theta}_{k+1} = \boldsymbol{\theta}_k - \eta \tilde{\mathbf{g}}_k, \quad (9)$$

where the gradient $\tilde{\mathbf{g}}_k$ is given in Eqn. (8). Now we are ready to analyze LoCo-integrated SGD and summarize the results in Theorem 1 with its proof in Appendix C.2.

Theorem 1 (SGD Convergence). *Suppose that Assumptions 1, 2, and 3 hold. Let $s_e = \Omega(\epsilon^{-4})$ and $\eta = \mathcal{O}(\epsilon^2)$ in LoCo-integrated SGD. Then, after $T = \Omega(\epsilon^{-4})$ iterations, we have:*

$$\frac{1}{T} \sum_{k=0}^T \mathbb{E} \|\nabla f(\boldsymbol{\theta}_k)\|^2 \leq \mathcal{O}(\epsilon^2).$$

That is, the stochastic gradient complexity to find an ϵ -accurate first-order stationary point is $\mathcal{O}(\epsilon^{-4})$.

Theorem 1 demonstrates that LoCo-integrated SGD and the original SGD exhibit identical convergence rates, with stochastic gradient complexity (i.e., the number of gradient evaluations) relative to ϵ , achieving the theoretical lower bound [48]. The advantageous properties of LoCo-integrated SGD arise from two key factors: 1) The refined EFC in LoCo ensures that gradient compression errors do not accumulate over iterations. As shown in Eqn. (6), both single-step and multi-step errors remain of the same order of magnitude; 2) LoCo's periodic error reset mechanism prevents the compression errors, when compressing the compensation error $\tilde{\mathbf{e}}_{k+1}^n$ to its 8-bit form \mathbf{e}_{k+1}^n , from accumulating over time. This reset mechanism ensures that these compression errors are eliminated after a finite number of steps. These properties ensure that the distance between the training sequences of LoCo-integrated SGD and the original SGD remains tightly bounded.

4.2 LoCo-integrated Adam-family Optimizers

The algorithmic steps for Adam-type optimizers are

$$\text{Adam Family: } \begin{cases} \mathbf{m}_k = (1 - \beta_1)\mathbf{m}_{k-1} + \beta_1 \tilde{\mathbf{g}}_k, \\ \boldsymbol{\eta}_k = \eta \times v(\tilde{\mathbf{g}}_0, \dots, \tilde{\mathbf{g}}_k), \\ \boldsymbol{\theta}_{k+1} = \boldsymbol{\theta}_k - \boldsymbol{\eta}_k \circ \mathbf{m}_k, \end{cases} \quad (10)$$

where \circ is the element-wise product, $\beta_1 \in (0, 1)$, and $\mathbf{m}_0 = \mathbf{0}$. For Adam Family, its operation $v(\cdot)$ is to compute the pre-conditioner, e.g., the inverse of Adam's second-order moment, $v(\tilde{\mathbf{g}}_0, \dots, \tilde{\mathbf{g}}_k) = 1/\sqrt{\mathbf{v}_k + \delta}$, where $\mathbf{v}_k = (1 - \beta_2)\mathbf{v}_{k-1} + \beta_2 \tilde{\mathbf{g}}_k^2$ with $\beta_2 \in (0, 1)$ and $\mathbf{v}_0 = \mathbf{0}$. So by choosing different operation $v(\cdot)$, Adam Family contains many prevent optimizers [47], e.g., Adam, Aadafactor [25], and AdamW [54], etc. Before showing the main results, we introduce an assumption regarding the operation $v(\cdot)$. It should be noted that this is not strictly an assumption, as the condition can be readily satisfied by appropriately setting a hyper-parameter for $v(\cdot)$.

Assumption 4 (Pre-conditioner). *The pre-conditioner is element-wise bounded, i.e., $c_l \leq \|v(\cdot)\|_\infty \leq c_u$. Additionally, the element-wise difference of successive pre-conditioners is bounded:*

$$\|v(\tilde{\mathbf{g}}_0, \dots, \tilde{\mathbf{g}}_k) - v(\tilde{\mathbf{g}}_0, \dots, \tilde{\mathbf{g}}_{k-1})\|_\infty \leq \beta_1 c_u,$$

where β_1 , as defined in Eqn. (10), represents the momentum for Adam-family methods.

Assumption 4 ensures that the pre-conditioner maintains appropriate bounds and does not fluctuate significantly during training. This requirement is commonly satisfied by several Adam-type optimizers. For instance, in Adam and AdamW, setting $v(\tilde{\mathbf{g}}_0, \dots, \tilde{\mathbf{g}}_k) = 1/\sqrt{\mathbf{v}_k + \delta}$, with $\mathbf{v}_k = (1 - \beta_2)\mathbf{v}_{k-1} + \beta_2 \tilde{\mathbf{g}}_k^2$, yields $c_u = 1/\sqrt{\delta}$. By choosing $\beta_2 = \mathcal{O}(\beta_1)$, the difference bound is always satisfied. In practice, it is typical to set $\beta_1 = 0.1$ and $\beta_2 \in [0.001, 0.05]$, thereby complying with Assumption 4. For further details on other Adam-type optimizers and their adherence to Assumption 4, please refer to the discussion in [47].

Theorem 2. *Suppose Assumptions 1, 2, 3, and 4 hold. Let $s_e = \Omega(\epsilon^{-4})$, $\eta = \mathcal{O}(\epsilon^2)$, and $\beta_1 = \mathcal{O}(\epsilon^2)$ in LoCo-integrated Adam-type optimizers, then after $T = \Omega(\epsilon^{-4})$ iterations, the following inequality holds:*

$$\frac{1}{T} \sum_{k=0}^{T-1} \mathbb{E} \left[\|\nabla f(\boldsymbol{\theta}_k)\|^2 + \frac{1}{4} \|\mathbf{m}_k\|^2 \right] \leq \epsilon^2. \quad (11)$$

That is, the stochastic gradient complexity is $\mathcal{O}(\epsilon^{-4})$.

Theorem 2 reveals an important insight: *integrating LoCo into various adaptive optimizers does not compromise their convergence speed.* Furthermore, Theorems 1 and 2 collectively show that LoCo-integrated optimizers exhibit the same stochastic gradient complexity as their vanilla counterparts. For instance, when aiming for an ϵ -accurate first-order stationary point (ϵ -FOSP) in a non-convex optimization problem, the complexity for both SGD and Adam-type optimizers, as well as their LoCo-integrated versions, remains $\mathcal{O}(\epsilon^{-4})$. This illustrates that LoCo preserves the convergence performance while utilizing low-bit gradients, thereby significantly enhancing communication efficiency.

4.3 Comparison of Communication-Efficient Methods

Here we compare LoCo with previous efficient training methods across five aspects: gradient complexity, communication time, memory overhead, RC support, and sharding support. The specific results are summarized in Table 1. Consistent with the Zero sharding method [28], we consider

TABLE 1: Comparison of LoCo with previous communication-efficient training methods across various metrics, including gradient complexity, communication time, memory overhead, RC support, and sharding support. Here, Ψ represents the number of model parameters, N_d is the number of distributed nodes, B is the communication bandwidth (bytes/s), and r is the low-rank parameter specific to PowerSGD. We consider the mixed-precision setting for memory overhead.

| Methods | Gradient Complexity | Communication Time | Memory Consumed | Ring-based Comm. | Opt. + Grad. Sharding |
|-------------------|------------------------------|---------------------------------|--------------------------|------------------|-----------------------|
| EF [17] | $\mathcal{O}(\epsilon^{-4})$ | $2.5\Psi N_d/B$ | 10Ψ | \times | \times |
| EF21 [18] | $\mathcal{O}(\epsilon^{-4})$ | $2.5\Psi N_d/B$ | 10Ψ | \times | \times |
| 1-bit Adam [14] | $\mathcal{O}(\epsilon^{-4})$ | $0.625\Psi N_d/B$ | 18Ψ | \times | \times |
| 1-bit LAMB [19] | $\mathcal{O}(\epsilon^{-4})$ | $0.625\Psi N_d/B$ | 22Ψ | \times | \times |
| PowerSGD [41] | \times | $4r\sqrt{\Psi}(N_d - 1)/(BN_d)$ | $14\Psi + 2r\sqrt{\Psi}$ | \checkmark | \checkmark |
| Modified EF-SGD | $\mathcal{O}(\epsilon^{-4})$ | $2.25\Psi(N_d - 1)/(BN_d)$ | $4\Psi + 6\Psi/N_d$ | \checkmark | \checkmark |
| Modified EF21-SGD | $\mathcal{O}(\epsilon^{-4})$ | $2.25\Psi(N_d - 1)/(BN_d)$ | $4\Psi + 10\Psi/N_d$ | \checkmark | \checkmark |
| Adam [24] | $\mathcal{O}(\epsilon^{-4})$ | $4\Psi(N_d - 1)/(BN_d)$ | $2\Psi + 14\Psi/N_d$ | \checkmark | \checkmark |
| SGD | $\mathcal{O}(\epsilon^{-4})$ | $4\Psi(N_d - 1)/(BN_d)$ | $2\Psi + 6\Psi/N_d$ | \checkmark | \checkmark |
| Adam-Zero++ [46] | \times | $2\Psi(N_d - 1)/(BN_d)$ | $2\Psi + 14\Psi/N_d$ | \checkmark | \checkmark |
| LoCo-SGD (ours) | $\mathcal{O}(\epsilon^{-4})$ | $2.25\Psi(N_d - 1)/(BN_d)$ | $3\Psi + 6\Psi/N_d$ | \checkmark | \checkmark |
| LoCo-Adam (ours) | $\mathcal{O}(\epsilon^{-4})$ | $2.25\Psi(N_d - 1)/(BN_d)$ | $3\Psi + 14\Psi/N_d$ | \checkmark | \checkmark |

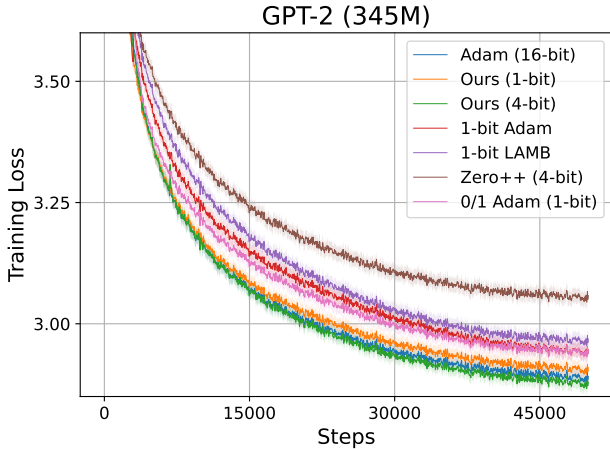


Fig. 2: Loss curve of various low-bit methods on GPT2-345M trained with 52B tokens from OpenWebtext dataset.

partitioning the optimizer states and gradients, i.e., the scenario of Zero2. Here, Ψ denotes the number of model parameters, N_d represents the number of nodes in distributed training (for master-server mode, N_d refers to the number of nodes computing local gradients), B is the communication bandwidth in bytes per second, and r is the low-rank parameter specific to PowerSGD [41]. We also evaluate modified EF and modified EF21, which adapt the original EF [17] and EF21 [18] methods for the popular sharding framework despite being originally designed for MSC.

For memory computation, we consider a mixed-precision training setting where 16-bit parameters and 16-bit gradients are present in memory (each consuming 2Ψ bytes). Additionally, for SGD and Adam optimizers, there is a 32-bit parameter copy (consuming 4Ψ bytes). Furthermore, Adam optimizers require an additional 8Ψ bytes to store first-order and second-order moments. The 1-bit LAMB [19] method requires an additional 4Ψ bytes for another second-order moment. EFC-based methods need extra memory to store the error (16-bit, consuming 2Ψ bytes, decoupled from optimizer states), whereas LoCo only requires an additional Ψ bytes, as

it stores the error in 8-bit format. Modified EF21 additionally needs to store a shared global error variable, which consumes $4\Psi/N_d$ bytes. PowerSGD, in addition to using EFC, requires extra memory to store a 16-bit low-rank matrix, consuming $2r\sqrt{\Psi}$ bytes. For sharding scenarios, we consider splitting gradients and optimizer states but not the 16-bit model parameters to avoid additional communication overhead.

Communication time in current deep learning settings usually involves two parts: gradient communication (reduce-scatter) and parameter synchronization (all-gather). For the MSC mode, gradients are sent to the master node, processed, and then returned to the nodes. The total communication time is $(b_g + b_w)\Psi N_d/8B$, where b_g and b_w are the bits used for communicating gradients and parameters/weights, respectively. For example, for 1-bit Adam and 1-bit LAMB, $b_g = 1$ and $b_w = 1$, noting that the first 10% of iteration steps use full-precision communication as a warm-up. For EF [17] and EF21 [18], $b_g = 4$ and $b_w = 16$.

For methods supporting RC, the total communication time is given by $(b_g + b_w)\Psi(N_d - 1)/(8N_dB)$. In this scheme, each node’s communication volume per step is $b\Psi/N_d$, requiring $(N_d - 1)$ steps to complete a full gradient or parameter exchange. Here, b represents the bit size used for communication. Specifically, for Adam and SGD, $b_g = 16$ and $b_w = 16$. For Zero++ (combined with Adam), $b_g = 8$ and $b_w = 8$. For LoCo, modified EF, and modified EF21, $b_g = 4$ and $b_w = 16$. For PowerSGD, the communication volume is $br\sqrt{\Psi}/N_d$, while other aspects remain similar to SGD.

From the results in Table 1, it is evident that LoCo demonstrates superior properties compared to other methods. LoCo supports both ring-based and sharding strategies, which keeps communication costs stable regardless of the number of GPUs and reduces memory overhead. This is particularly advantageous over methods like EF21 and PowerSGD, which incur higher memory usage due to a lack of sharding support, and MSC-based methods such as 1-bit Adam and 1-bit LAM, whose communication time increases with more nodes. Therefore, LoCo is more suitable for training large-

TABLE 2: Comparison between 16-bit Adam and 4-bit LoCo with Adam as base optimizer, which respectively uses 16- and 4-bit gradient for communication. The tasks include commonsense reasoning, world knowledge, mathematics, coding, etc.

| Model | Optimizer | MMLU | HellaS | WinoG | PIQA | Arc-e | Arc-c | NQ | TriQA | HumanE | MBPP | Math | GSM8K | Avg. |
|-------------------|------------|--------------|--------------|--------------|--------------|--------------|--------------|--------------|--------------|--------------|--------------|--------------|--------------|---------------|
| LLAMA2 (7B) | Adam | 46.0% | 74.3% | 62.3% | 77.7% | 59.2% | 43.3% | 14.0% | 51.1% | 13.4% | 15.8% | 3.1% | 16.8% | 39.75% |
| | Adam+LoCo | 46.2% | 74.3% | 62.2% | 77.8% | 58.6% | 44.1% | 13.4% | 50.8% | 13.5% | 14.8% | 3.2% | 17.5% | 39.70% |
| LLAMA2 (13B) | Adam | 55.2% | 77.7% | 64.0% | 79.8% | 74.7% | 58.9% | 15.6% | 56.9% | 20.1% | 28.6% | 5.2% | 29.1% | 47.15% |
| | Adam+LoCo | 55.2% | 77.7% | 64.3% | 79.8% | 74.8% | 58.6% | 15.5% | 57.2% | 19.5% | 28.6% | 5.4% | 30.1% | 47.22% |
| Mixtral (8×7B) | AdamW | 70.1% | 82.0% | 70.1% | 83.3% | 94.0% | 86.1% | 31.1% | 65.5% | 34.7% | 42.4% | 22.9% | 70.4% | 62.71% |
| | AdamW+LoCo | 70.3% | 81.7% | 69.7% | 83.1% | 94.7% | 86.8% | 31.1% | 64.6% | 36.6% | 41.6% | 23.2% | 69.5% | 62.74% |

TABLE 3: The fine-tuning losses of 4-bit LoCo and the 16-bit communication based optimizers on LLAMA2 and Mixtral.

| Model | Optimizer | Loss | Baseline | LoCo |
|-------------------|-----------|-------|---------------|---------------|
| LLAMA2 (7B) | Adam | Train | 1.688 | 1.688 |
| | | Val. | 1.503 | 1.503 |
| LLAMA2 (13B) | Adam | Train | 1.612 | 1.612 |
| | | Val. | 1.415 | 1.415 |
| Mixtral (8×7B) | AdamW | Train | 0.7041 | 0.7030 |
| | | Val. | 0.7038 | 0.7030 |
| Mixtral (8×7B) | Adafactor | Train | 0.6123 | 0.6117 |
| | | Val. | 0.6206 | 0.6207 |

TABLE 4: Comparison of training loss for Sky-MoE with different data volumes and model sizes using LoCo (4-bit) and full-precision Adam.

| Models | Token Size | Model Size | Adam | Adam+LoCo |
|--------------|------------|------------|--------------|--------------|
| Sky-MoE [55] | 10B | 8 × 0.1B | 2.635 | 2.636 |
| | 30B | 8 × 0.1B | 2.477 | 2.475 |
| | 300B | 8 × 0.3B | 2.105 | 2.102 |

scale models, offering both efficient communication and small memory costs. Although LoCo does not show a clear advantage over Zero++ in terms of communication time and memory overhead, the latter lacks convergence guarantees, potentially impacting training quality, as verified in Fig. 2 and Table 5. Methods without convergence guarantees tend to underperform.

Despite the ability of original EF and EF21 to adapt to the sharding framework, they consume additional memory compared to LoCo. For instance, modified EF21 requires extra storage for a shared global error variable, increasing the optimizer’s 32-bit state size. Moreover, our experiments indicate that merely adapting EFC to the sharding framework can lead to significant performance degradation. Without the improvements proposed in LoCo, such as error averaging and error resetting, training performance can suffer drastically, even failing in pre-training experiments (see Sec. 5.2) or showing subpar results in fine-tuning (see Table 9).

Finally, compared to the original Adam or SGD, LoCo achieves significant communication efficiency improvements with small additional memory overhead while maintaining the same convergence speed. In large-scale experiments, the speedup can reach 1.4x or more, with less than 10% additional memory overhead. This memory overhead is even negligible in some cases, such as in LLM with large batch sizes and token lengths (see Table 7 and 8).

5 EXPERIMENTS

To test LoCo, we first compare it with several representative baselines, including low-bit optimizers with error-feedback like 1-bit Adam [14], and quantization method like Zero++ [46]. Moreover, we further compare LoCo with the widely used 16-bit optimizers, e.g., Adam [24], AdamW [54], and Adafactor [25]. Subsequently, we examine the training speed of LoCo across diverse model architectures, model sizes, GPU server configurations, and large-model training frameworks. Finally, we investigate the effect of each key component in LoCo. See detailed experimental settings in Appendix B.

5.1 Results on LoCo-Integrated Optimizers

We integrate LoCo (4-bit) into various optimizers, including Adam, AdamW [54], and Adafactor, and compare with the corresponding 16-bit counterparts. For evaluation, we use these optimizers to train two advanced LLMs, LLAMA2 and Mixtral, under the RC setting. For LLAMA2, we follow [56] to use the RedPajama subset for fine-tuning on 8B tokens. For Mixtral, following [57], we adopt ultra-chat-200k dataset [58] to fine-tune for one epoch. These fine-tuning protocols are to align with the established benchmarks, and provide convincing assessment to LoCo.

Fine-tuning results on LLAMA2 and Mixtral (8x7B).

Table 3 shows that 4-bit LoCo-integrated optimizers enjoy similar training and validation losses with their corresponding 16-bit counterparts on LLAMA2 and Mixtral, indicating their similar convergence speed and training quality. From Table 2, one can see that when evaluated on downstream tasks, 4-bit LoCo-integrated optimizers share comparable performance as their corresponding 16-bit ones, and even occasionally exceed them. All these results affirm the effectiveness of LoCo on the large-model training setting.

5.2 SoTA Comparison Under Low-bit Communication

Here we compare LoCo with communication-efficient methods including 1-bit Adam, 1-bit LAMB [19], 0/1 Adam [15] and Zero++. Among them, 1-bit Adam, 1-bit LAMB, and 0/1 Adam design error-feedback strategies for server-worker settings and cannot be directly applied to ring-based communication settings. Zero++ only compresses its gradient into low-bit ones without any error-feedback strategy and could suffer from information loss. For LoCo, we combine it with Adam for fairness.

Results on MoE trained from scratch. To validate the effectiveness of LoCo on large-scale datasets, we conducted training-from-scratch experiments on the popular MoE model [26], [55]. These experiments spanned various data volumes and model sizes. Specifically, we trained two configurations of the Sky-MoE [55] with 8 experts: 8 × 0.1B (total

TABLE 5: Performance comparison of representative low-bit communication methods. We fine-tune LLAMA2-7B on the alpaca-gpt4 dataset. The downstream tasks include commonsense reasoning, world knowledge, mathematics, and coding.

| Method | HumanE | MBPP | GSM8K | NQ | HellaS | Arc-e | Arc-c | PIQA | WinoG | MMLU | Avg. |
|-------------------|--------|-------|-------|-------|--------|-------|-------|-------|-------|-------|-------|
| Adam (16-bit) | 16.4% | 20.0% | 15.7% | 14.6% | 75.4% | 73.5% | 52.2% | 78.6% | 61.4% | 48.0% | 45.6% |
| 0/1 Adam (4-bit) | 15.2% | 21.0% | 11.8% | 13.3% | 74.9% | 74.6% | 50.5% | 78.0% | 61.2% | 47.7% | 44.8% |
| 4-bit Adam | 15.3% | 19.4% | 13.4% | 14.4% | 74.5% | 74.8% | 47.1% | 78.2% | 61.7% | 47.2% | 44.6% |
| 4-bit LAMB | 17.6% | 22.0% | 15.2% | 13.0% | 75.2% | 71.0% | 50.5% | 78.5% | 61.5% | 47.8% | 45.2% |
| Zero++ (4-bit) | 15.9% | 17.6% | 13.6% | 14.0% | 75.8% | 72.5% | 46.1% | 78.0% | 61.9% | 47.1% | 44.3% |
| Adam+LoCo (4-bit) | 16.5% | 21.8% | 15.6% | 13.9% | 76.1% | 72.9% | 51.4% | 78.3% | 61.8% | 48.0% | 45.6% |

TABLE 6: Comparison of fine-tuning results using LoRA on the LLaMA2-7B model with Alpaca-GPT4 dataset.

| Method | HumanE | MBPP | GSM8K | HellaS | Arc-e | Arc-c | PIQA | WinoG | MMLU | Avg. |
|----------------|--------|-------|-------|--------|-------|-------|-------|-------|-------|-------|
| AdamW (16-bit) | 13.4% | 17.4% | 16.2% | 73.9% | 59.8% | 44.4% | 77.9% | 62.6% | 45.9% | 45.7% |
| PowerSGD | 13.2% | 19.0% | 16.9% | 73.4% | 58.1% | 43.1% | 77.2% | 62.5% | 45.7% | 45.4% |
| AdamW+LoCo | 13.0% | 17.2% | 16.7% | 73.8% | 59.9% | 44.4% | 77.6% | 62.4% | 45.9% | 45.7% |

TABLE 7: Training speed (throughput) investigation of LoCo in prevalent Megatron-LM framework for efficient multi-node LLMs training with different model sizes, GPU number, and the node connection.

| Model | 32× NVIDIA A100 (RoCE v2) | | | 64× NVIDIA A100 (RoCE v2) | | | 128× NVIDIA A100 (RoCE v2) | | |
|---------------------|-----------------------------------|--------------------|----------------|------------------------------|--------------------|----------------|-------------------------------|--------------------|----------------|
| | BP16 (tokens/s) | Ours (tokens/s) | Speedup (%) | BP16 (tokens/s) | Orus (tokens/s) | Speedup (%) | BP16 (tokens/s) | Ours (tokens/s) | Speedup (%) |
| LLAMA2 (7B) | 57230.2 | 65376.3 | 14.23 | 108680.5 | 127263.1 | 17.10 | 212373.9 | 251701.9 | 18.50 |
| Mistral (7B) | 55947.3 | 64123.7 | 14.61 | 105198.2 | 125422.7 | 19.22 | 206053.7 | 247468.3 | 20.10 |
| LLAMA2 (13B) | 30555.9 | 35683.2 | 16.78 | 43941.6 | 55322.9 | 25.90 | 83160.2 | 108577.2 | 30.56 |
| LLAMA2 (70B) | N/A, since the Data Parallel is 1 | | | 2869.2 | 3803.2 | 32.55 | 5263.6 | 7107.6 | 35.03 |
| | 32× NVIDIA A800 (Infiniband) | | | 64× NVIDIA A800 (Infiniband) | | | 128× NVIDIA A800 (Infiniband) | | |
| LLAMA2 (7B) | 54186.8 | 65862.1 | 21.55 | 89555.4 | 120625.6 | 34.69 | 161447.6 | 224887.7 | 39.29 |
| Mistral (7B) | 51896.8 | 63568.5 | 22.49 | 85334.5 | 115355.6 | 35.18 | 155308.7 | 217494.4 | 40.04 |
| LLAMA2 (13B) | 30682.9 | 38226.1 | 24.58 | 49907.4 | 69409.0 | 39.08 | 90446.3 | 128649.6 | 42.24 |

TABLE 8: Comparison of peak memory of LoCo (4-bit) and Adam (16-bit) on various settings with 32 GPUs.

| Model | Framework | Peak Memory (GB) | |
|--------------------|-------------|------------------|-----------|
| | | Adam | Adam+LoCo |
| Mixtral (8 × 7B) | FSDP | 58.8 | 64.3 |
| LLAMA2-7B | FSDP | 20.5 | 22.7 |
| Sky-MoE (8 × 0.1B) | Megatron-LM | 72.3 | 72.7 |
| Sky-MoE (8 × 0.3B) | Megatron-LM | 56.3 | 57.0 |
| LLAMA2-7B | Megatron-LM | 44.0 | 48.1 |
| LLAMA2-13B | Megatron-LM | 68.3 | 74.5 |

parameter count of 0.5B) and 8×0.3 (total parameter count of 2B), using tokens from the RedPajama-v2 dataset [59] in sizes of 10B, 30B, and 300B. We report the training loss, which is equivalent to the validation loss in this context, as the model encounters each data point only once during training. In this experiment, we applied element-wise clipping to the estimated local gradient g_k^n to reduce sensitivity to the compression hyperparameter s in LoCo.

As shown in Table 4, despite utilizing 4-bit gradient communication, LoCo achieved results consistent with full-precision Adam across different data volumes and model sizes. Unlike fine-tuning, training from scratch on large datasets better demonstrates the practical utility and communication efficiency of LoCo.

Results on GPT2 trained from scratch. We train GPT2-

345M on the OpenWebtext dataset [60] of 52B tokens from scratch. Fig. 2 shows that 1) our 1-bit LoCo has faster convergence speed than 1-bit optimizers, and 2) our 4-bit LoCo even share similar behaviors as 16-bit Adam and is better than our 1-bit version. So without sacrificing performance, LoCo can improve communication efficiency, showing the superiority of our error-feedback strategy in maintaining training quality.

Results on LLAMA2-7B fine-tuned on downstream tasks. We follow [61] and fine-tune LLAMA2-7B for three epochs on the alpaca-gpt4 dataset to evaluate commonsense reasoning ability. Here, we use the 4-bit gradient in 1-bit Adam, 0/1 Adam, since we find that they are very unstable during training billion-scale models.

Table 5 reveals that LoCo outperforms all 4-bit optimizers, e.g., 0/1 Adam and Zero++, and even achieves comparable performance as 16-bit Adam, the official optimizer, on all commonsense reasoning tasks. This well demonstrates the training quality of LoCo, which only uses a 4-bit gradient. Moreover, other 4-bit optimizers often have much worse performance than 16-bit Adam. This is because their error-feedback indeed cannot well address the accumulated gradient quantization error over the iterations, while LoCo introduces the moving average to stabilize the fluctuating quantization error and also restart the error to remove the impact from the out-of-date historical error.

Results on LLAMA2-7B trained with LoRA [62]. To compare LoCo with other efficient communication methods,

TABLE 9: Effects of the different components in LoCo to the performance on LLAMA2-7B fine-tuned on the alpaca-gpt4 dataset, including error-feedback, error compression, moving average on errors, and periodic error resetting. LoCo is integrated with Adam.

| Method | Error Feedback | Error Cmpr. | Err. Reset Freq. | Err. Avg. | HumanE | MBPP | GSM8K | Math | HellaS | Arc-e | Arc-c | PIQA | WinoG | MMLU | Avg. |
|--------|----------------|-------------|------------------|-----------|--------|-------|-------|-------|--------|-------|-------|-------|-------|-------|-------|
| LoCo1 | ✗ | N/A | N/A | ✗ | 49.0% | 50.0% | 67.2% | 23.0% | 81.7% | 94.0% | 87.4% | 82.6% | 68.7% | 70.8% | 67.4% |
| LoCo2 | ✓ | ✓ | N/A | ✗ | 48.8% | 49.6% | 67.6% | 23.7% | 81.8% | 93.9% | 87.5% | 82.6% | 68.3% | 70.9% | 67.5% |
| LoCo3 | ✓ | ✓ | N/A | ✓ | 49.4% | 50.4% | 67.3% | 23.5% | 81.8% | 94.0% | 87.8% | 83.1% | 69.5% | 70.9% | 67.7% |
| LoCo4 | ✓ | ✗ | 512 | ✓ | 51.8% | 50.0% | 66.5% | 22.9% | 82.2% | 93.8% | 87.8% | 83.3% | 69.5% | 70.4% | 67.8% |
| LoCo5 | ✓ | ✓ | 512 | ✓ | 51.8% | 50.0% | 67.9% | 23.2% | 81.8% | 94.0% | 87.8% | 83.1% | 68.8% | 71.0% | 67.9% |
| LoCo6 | ✓ | ✓ | 128 | ✓ | 53.1% | 50.2% | 67.3% | 23.5% | 81.8% | 94.0% | 87.4% | 83.2% | 69.1% | 71.0% | 68.1% |

TABLE 10: Speedup achieved by LoCo against 16-bit communication within the PyTorch FSDP framework for MoE model on an NVIDIA A800 cluster with Infiniband connectivity.

| Model | GPU Number | BP16 (tokens/s) | LoCo (tokens/s) | Speedup (%) |
|----------------|------------|-----------------|-----------------|-------------|
| Mixtral (8×7B) | 32 | 14356.1 | 18357.4 | 27.87 |
| | 64 | 25450.9 | 34044.7 | 33.77 |

such as PowerSGD, without model sharding, we utilized the LoRA [62] strategy for fine-tuning (as full-parameter fine-tuning under DDP mode would result in out-of-memory). We fine-tuned the LLaMA2-7B model on the Alpaca-GPT4 dataset. The results, presented in Table 6, indicate that PowerSGD underperforms compared to LoCo and exhibits a gap from the baseline. In contrast, LoCo achieves results comparable to 16-bit full-precision AdamW. Although PowerSGD can reduce communication overhead by adjusting the low-rank parameter r , its convergence is challenging to ensure. Additionally, PowerSGD lacks support for FSDP, leading to substantial memory overhead, making full-parameter fine-tuning impractical.

5.3 Results on Training Speed

Here, we investigate the training speed of LoCo by reporting its throughput (i.e., the number of consumed tokens per second) under different settings. For comprehensive investigation, we test LoCo by using different model architectures, node connections, and large-model training frameworks. We report the throughput of the popular LLAMA2, Mistral, and Mixtral (i.e., MoE-Mistral) on both the A100 cluster interconnected with RoCE network and the A800 cluster interconnected with Infiniband. Due to limited space, we defer more training speed results in Appendix B.1. *For LoCo, we combine it with Adam for fairness.*

Model architectures. Table 7 reveals that on all LLMs whose size varies from 7B to 70B, LoCo makes a significant speedup on the official 16-bit Adam in terms of the throughput. Moreover, the larger the model, the greater LoCo speeds up. For example, LoCo achieves a speedup of 35.03% for 70B LLAMA2 on 128 A100 GPUs and 42.24% for 13B LLAMA2 on 128 A800 GPUs. This shows the good scalability of LoCo.

GPU types. Table 7 shows that the lower the bandwidth of a cluster, the more significant improvement LoCo can achieve. The A800 cluster has a lower bandwidth than the A100 cluster and shows a greater speedup. For instance, on 7B Mistral, LoCo has a 22.49% improvement on the A800 server but has a 14.61% improvement on the A100 cluster.

Moreover, the more GPUs in a cluster, the more speedup LoCo makes. For example, as shown in Table 7, on 13B LLAMA2, the speedup of LoCo is improved from 24.58% to 42.24% when the GPU number increases from 32 to 128 on the A800 server. This is because if a server’s bandwidth becomes smaller or its GPU number increases, its communication cost (including volume and round) will increase and become the training bottleneck, leading to slow training speed. For these cases, LoCo can greatly reduce communication costs by using the low-bit gradient, thus significantly improving the training speed.

Large-scale training frameworks. Table 7 evaluates LoCo via Megatron-LM training framework [13], while Table 10 focuses the speed on PyTorch FSDP framework [16]. Megatron-LM uses comprehensive parallelizations to improve training efficiency, e.g., data, pipeline, and tensor parallelism, and is widely used in LLMs training, while FSDP enhances efficiency by partitioning model, gradients, and optimizer states, and improves the communication efficiency during back-propagation. Table 7 and Table 10 show that on both frameworks, LoCo makes notable speed up and shows its high compatibility.

Peak memory comparison. Table 8 shows that LoCo often requires only an additional 9-10% memory overhead compared with the official 16-bit Adam for both LLAMA2 and Mixtral. For practical LLM training, GPU memory is often not fully used since selecting a widely used and proper maximum token length to use GPU memory fully is hard, making some extra GPU memory available. In this way, the remaining available GPU memory can be used for the extra 10% memory cost in LoCo. Moreover, as shown in Table 7, LoCo often brings 15% to 40% overall training speedup.

5.4 Ablation Experiments

We delve into the effects of various components of LoCo, including 1) error-feedback, 2) moving averaging on error, 3) error compression, and 4) error reset. We follow Sec. B.2 to fine-tune Mixtral. Table 9 reports the results of LoCo with Adam as its optimizer.

Error-feedback. By comparing LoCo1 and LoCo2 in Table 9, one can observe that incorporating error-feedback directly almost does not bring improvement. Specifically, integrating error-feedback slightly impairs the performance on the coding-related benchmarks, e.g., HumanE and MBPP. This may be attributed to the discontinuity in compression, which results in significant variance for compression error. Hence, we still need other components of LoCo to boost the performance jointly.

Moving average on error. To mitigate instability in vanilla error-feedback which solely uses compression error from one previous iteration, we design a moving average on all historical compression errors to estimate more stable and accurate compression error. LoCo2 and LoCo3 in Table 9 shows that moving average on error improves a lot on downstream tasks, particularly in coding-related benchmarks.

Error compression. To save GPU memory, we compress high-precision compensation errors into 8-bit ones. By comparing LoCo4 and LoCo5 in Table 9, this compression only brings negligible performance degradation while further reducing the memory footprint of LoCo. This enhances the applicability of LoCo for large-model training.

Error reset. Along with the training, the very early compensation errors become outdated and is not suitable for current estimation. So we design an error reset mechanism, a critical element in both theoretical and practical realms. Our theoretical analysis, particularly in the proofs of Theorems 1, highlights the significance of periodic error resets in controlling the error scale and ensuring algorithmic convergence. In practice, By comparing LoCo5 and LoCo6 in Table 9, setting the error reset frequency (T_c) to either 128 or 512 has shown notable performance boosts. This error resetting strategy ensures an accurate estimation, and aligns with our theoretical findings, thereby enhancing the effectiveness of LoCo. Notably, for simplicity, we always set the reset frequency as 512 in all other experiments.

6 CONCLUSION

LoCo addresses the challenges of efficient large-model training with low-precision gradient communication. It successfully compensates gradients before compression, ensuring effective communication without sacrificing training quality. Distinguished by its low computational and memory requirements, LoCo advances beyond traditional compression methods by preventing error accumulation during the optimization process. Its compatibility with various optimizers and gradient partitioning techniques in advanced training frameworks demonstrates its versatility and practical utility.

REFERENCES

- [1] T. Brown, B. Mann, N. Ryder, M. Subbiah, J. D. Kaplan, P. Dhariwal *et al.*, "Language models are few-shot learners," *Advances in neural information processing systems*, vol. 33, pp. 1877–1901, 2020.
- [2] A. Q. Jiang, A. Sablayrolles, A. Mensch, C. Bamford, D. S. Chaplot, D. d. l. Casas *et al.*, "Mistral 7b," *arXiv preprint arXiv:2310.06825*, 2023.
- [3] Y. Bai, X. Geng, K. Mangalam, A. Bar, A. Yuille, T. Darrell *et al.*, "Sequential modeling enables scalable learning for large vision models," *arXiv preprint arXiv:2312.00785*, 2023.
- [4] H. Liu, C. Li, Q. Wu, and Y. J. Lee, "Visual instruction tuning," *arXiv preprint arXiv:2304.08485*, 2023.
- [5] A. Radford, J. Wu, R. Child, D. Luan, D. Amodei, I. Sutskever *et al.*, "Language models are unsupervised multitask learners," *OpenAI blog*, vol. 1, no. 8, p. 9, 2019.
- [6] H. Touvron, T. Lavril, G. Izacard, X. Martinet, M.-A. Lachaux, T. Lacroix, B. Rozière *et al.*, "Llama: Open and efficient foundation language models," *arXiv preprint arXiv:2302.13971*, 2023.
- [7] H. Touvron, L. Martin, K. Stone, P. Albert, A. Almahairi, Y. Babaei *et al.*, "Llama 2: Open foundation and fine-tuned chat models," *arXiv preprint arXiv:2307.09288*, 2023.
- [8] S. Wu, O. Irsoy, S. Lu, V. Dabrovolski, M. Dredze, S. Gehrmann *et al.*, "Bloomberggpt: A large language model for finance," *arXiv preprint arXiv:2303.17564*, 2023.
- [9] Z. Sun, "A short survey of viewing large language models in legal aspect," *arXiv preprint arXiv:2303.09136*, 2023.
- [10] H. Zhou, B. Gu, X. Zou, Y. Li, S. S. Chen, P. Zhou *et al.*, "A survey of large language models in medicine: Progress, application, and challenge," *arXiv preprint arXiv:2311.05112*, 2023.
- [11] J. Dean, G. Corrado, R. Monga, K. Chen, M. Devin, M. Mao *et al.*, "Large scale distributed deep networks," *Advances in Neural Information Processing Systems*, vol. 25, 2012.
- [12] A. Harlap, D. Narayanan, A. Phanishayee, V. Seshadri, N. Devanur, G. Ganger *et al.*, "Pipedream: Fast and efficient pipeline parallel DNN training," *arXiv preprint arXiv:1806.03377*, 2018.
- [13] M. Shoenybi, M. Patwary, R. Puri, P. LeGresley, J. Casper, and B. Catanzaro, "Megatron-lm: Training multi-billion parameter language models using model parallelism," *arXiv preprint arXiv:1909.08053*, 2019.
- [14] H. Tang, S. Gan, A. A. Awan, S. Rajbhandari, C. Li, X. Lian *et al.*, "1-bit adam: Communication efficient large-scale training with adam's convergence speed," in *International Conference on Machine Learning*. PMLR, 2021, pp. 10 118–10 129.
- [15] Y. Lu, C. Li, M. Zhang, C. De Sa, and Y. He, "Maximizing communication efficiency for large-scale training via 0/1 adam," *arXiv preprint arXiv:2202.06009*, 2022.
- [16] Y. Zhao, A. Gu, R. Varma, L. Luo, C.-C. Huang, M. Xu *et al.*, "Pytorch fsdp: experiences on scaling fully sharded data parallel," *arXiv preprint arXiv:2304.11277*, 2023.
- [17] F. Seide, H. Fu, J. Droppo, G. Li, and D. Yu, "1-bit stochastic gradient descent and its application to data-parallel distributed training of speech dnns," in *Fifteenth Annual Conference of the International Speech Communication Association*, 2014.
- [18] P. Richtárik, I. Sokolov, and I. Fatkhullin, "EF21: A new, simpler, theoretically better, and practically faster error feedback," *Advances in Neural Information Processing Systems*, vol. 34, pp. 4384–4396, 2021.
- [19] C. Li, A. A. Awan, H. Tang, S. Rajbhandari, and Y. He, "1-bit LAMB: communication efficient large-scale large-batch training with lamb's convergence speed," in *IEEE 29th International Conference on High Performance Computing, Data, and Analytics*, 2022, pp. 272–281.
- [20] H. Tang, C. Yu, X. Lian, T. Zhang, and J. Liu, "Doublesqueeze: Parallel stochastic gradient descent with double-pass error-compensated compression," in *International Conference on Machine Learning*. PMLR, 2019, pp. 6155–6165.
- [21] K. Gruntkowska, A. Tyurin, and P. Richtárik, "EF21-p and friends: Improved theoretical communication complexity for distributed optimization with bidirectional compression," in *International Conference on Machine Learning*. PMLR, 2023, pp. 11 761–11 807.
- [22] P. Patarasuk and X. Yuan, "Bandwidth optimal all-reduce algorithms for clusters of workstations," *Journal of Parallel and Distributed Computing*, vol. 69, no. 2, pp. 117–124, 2009.
- [23] K. Mishchenko, B. Wang, D. Kovalev, and P. Richtárik, "Intsgd: Adaptive floatless compression of stochastic gradients," in *International Conference on Learning Representations*, 2021.
- [24] D. P. Kingma and J. Ba, "Adam: A method for stochastic optimization," *arXiv preprint arXiv:1412.6980*, 2014.
- [25] N. Shazeer and M. Stern, "Adafactor: Adaptive learning rates with sublinear memory cost," in *International Conference on Machine Learning*. PMLR, 2018, pp. 4596–4604.
- [26] A. Q. Jiang, A. Sablayrolles, A. Roux, A. Mensch, B. Savary, C. Bamford *et al.*, "Mixtral of experts," *arXiv preprint arXiv:2401.04088*, 2024.
- [27] D. Narayanan, M. Shoenybi, J. Casper, P. LeGresley, M. Patwary, V. Korthikanti *et al.*, "Efficient large-scale language model training on GPU clusters using Megatron-LM," in *Proceedings of the International Conference for High Performance Computing, Networking, Storage and Analysis*, 2021, pp. 1–15.
- [28] S. Rajbhandari, J. Rasley, O. Ruwase, and Y. He, "Zero: Memory optimizations toward training trillion parameter models," in *International Conference for High Performance Computing, Networking, Storage and Analysis*, 2020, pp. 1–16.
- [29] D. Alistarh, D. Grubic, J. Li, R. Tomioka, and M. Vojnovic, "Qsgd: Communication-efficient sgd via gradient quantization and encoding," *Advances in neural information processing systems*, vol. 30, 2017.
- [30] W. Wen, C. Xu, F. Yan, C. Wu, Y. Wang, Y. Chen *et al.*, "Terngrad: Ternary gradients to reduce communication in distributed deep learning," *Advances in neural information processing systems*, vol. 30, 2017.

- [31] J. Wangni, J. Wang, J. Liu, and T. Zhang, "Gradient sparsification for communication-efficient distributed optimization," *Advances in Neural Information Processing Systems*, vol. 31, 2018.
- [32] H. Wang, S. Sievert, S. Liu, Z. Charles, D. Papailiopoulos, and S. Wright, "Atomo: Communication-efficient learning via atomic sparsification," *Advances in Neural Information Processing Systems*, vol. 31, 2018.
- [33] S. Shi, X. Zhou, S. Song, X. Wang, Z. Zhu, X. Huang *et al.*, "Towards scalable distributed training of deep learning on public cloud clusters," *Proceedings of Machine Learning and Systems*, vol. 3, pp. 401–412, 2021.
- [34] X. Lian, C. Zhang, H. Zhang, C.-J. Hsieh, W. Zhang, and J. Liu, "Can decentralized algorithms outperform centralized algorithms? a case study for decentralized parallel stochastic gradient descent," *Advances in neural information processing systems*, vol. 30, 2017.
- [35] Y. Lu and C. De Sa, "Optimal complexity in decentralized training," in *International Conference on Machine Learning*. PMLR, 2021, pp. 7111–7123.
- [36] H. Zhao, B. Li, Z. Li, P. Richtárik, and Y. Chi, "Beer: Fast $o(1/t)$ rate for decentralized nonconvex optimization with communication compression," *Advances in Neural Information Processing Systems*, vol. 35, pp. 31 653–31 667, 2022.
- [37] Z. Li, D. Kovalev, X. Qian, and P. Richtárik, "Acceleration for compressed gradient descent in distributed and federated optimization," *arXiv preprint arXiv:2002.11364*, 2020.
- [38] Z. Li and P. Richtárik, "A unified analysis of stochastic gradient methods for nonconvex federated optimization," *arXiv preprint arXiv:2006.07013*, 2020.
- [39] J. Duchi, E. Hazan, and Y. Singer, "Adaptive subgradient methods for online learning and stochastic optimization," *Journal of machine learning research*, vol. 12, no. 7, 2011.
- [40] X. Xie, P. Zhou, H. Li, Z. Lin, and S. Yan, "Adan: Adaptive nesterov momentum algorithm for faster optimizing deep models," *IEEE Transactions on Pattern Analysis and Machine Intelligence*, 2024.
- [41] T. Vogels, S. P. Karimireddy, and M. Jaggi, "PowerSGD: Practical low-rank gradient compression for distributed optimization," *Advances in Neural Information Processing Systems*, vol. 32, 2019.
- [42] I. Fatkhullin, A. Tyurin, and P. Richtárik, "Momentum provably improves error feedback!" *Advances in Neural Information Processing Systems*, vol. 36, 2024.
- [43] H. Peng, K. Wu, Y. Wei, G. Zhao, Y. Yang, Z. Liu *et al.*, "Fp8-lm: Training fp8 large language models," *arXiv preprint arXiv:2310.18313*, 2023.
- [44] D. Alistarh, T. Hoefler, M. Johansson, N. Konstantinov, S. Khirirat, and C. Renggli, "The convergence of sparsified gradient methods," *Advances in Neural Information Processing Systems*, vol. 31, 2018.
- [45] S. U. Stich, J.-B. Cordonnier, and M. Jaggi, "Sparsified sgd with memory," *Advances in Neural Information Processing Systems*, vol. 31, 2018.
- [46] G. Wang, H. Qin, S. A. Jacobs, C. Holmes, S. Rajbhandari, O. Ruwase *et al.*, "Zero++: Extremely efficient collective communication for giant model training," *arXiv preprint arXiv:2306.10209*, 2023.
- [47] Z. Guo, Y. Xu, W. Yin, R. Jin, and T. Yang, "A novel convergence analysis for algorithms of the Adam family," *arXiv preprint arXiv:2112.03459*, 2021.
- [48] Y. Arjevani, Y. Carmon, J. C. Duchi, D. J. Foster, N. Srebro, and B. Woodworth, "Lower bounds for non-convex stochastic optimization," *Mathematical Programming*, pp. 1–50, 2022.
- [49] P. Zhou, X. Xie, Z. Lin, K.-C. Toh, and S. Yan, "Win: Weight-decay-integrated nesterov acceleration for faster network training," *Journal of Machine Learning Research*, vol. 25, no. 83, pp. 1–74, 2024.
- [50] P. Zhou, X. Xie, Z. Lin, and S. Yan, "Towards understanding convergence and generalization of adamw," *IEEE Transactions on Pattern Analysis and Machine Intelligence*, 2024.
- [51] Y. Zhang, C. Chen, N. Shi, R. Sun, and Z.-Q. Luo, "Adam can converge without any modification on update rules," *Advances in Neural Information Processing Systems*, vol. 35, pp. 28 386–28 399, 2022.
- [52] H. Li and Z. Lin, "On the $\mathcal{O}\left(\frac{\sqrt{d}}{T^{1/4}}\right)$ convergence rate of rmsprop and its momentum extension measured by ℓ_1 norm: Better dependence on the dimension," *arXiv preprint arXiv:2402.00389*, 2024.
- [53] A. Ajalloeian and S. U. Stich, "On the convergence of sgd with biased gradients," *arXiv preprint arXiv:2008.00051*, 2020.
- [54] I. Loshchilov and F. Hutter, "Decoupled weight decay regularization," in *International Conference on Learning Representations*, 2018.
- [55] L. Zhao, T. Wei, L. Zeng, C. Cheng, L. Yang, P. Cheng *et al.*, "Longskywork: A training recipe for efficiently extending context length in large language models," *arXiv preprint arXiv:2406.00605*, 2024. [Online]. Available: <https://arxiv.org/abs/2406.00605>
- [56] P. Zhang, G. Zeng, T. Wang, and W. Lu, "Tinyllama: An open-source small language model," 2024.
- [57] R. Zhang, J. Han, C. Liu, P. Gao, A. Zhou, X. Hu *et al.*, "Llama-adapter: Efficient finetuning of language models with zero-init attention," *arXiv preprint arXiv:2303.16199*, 2023.
- [58] N. Ding, Y. Chen, B. Xu, Y. Qin, Z. Zheng, S. Hu *et al.*, "Enhancing chat language models by scaling high-quality instructional conversations," 2023.
- [59] T. Computer, "Redpajama: an open dataset for training large language models," 2023. [Online]. Available: <https://github.com/togethercomputer/RedPajama-Data>
- [60] A. Gokaslan, V. Cohen, E. Pavlick, and S. Tellex, "Openwebtext corpus," 2019.
- [61] B. Peng, C. Li, P. He, M. Galley, and J. Gao, "Instruction tuning with gpt-4," *arXiv preprint arXiv:2304.03277*, 2023.
- [62] E. J. Hu, P. Wallis, Z. Allen-Zhu, Y. Li, S. Wang, L. Wang, *et al.*, "Lora: Low-rank adaptation of large language models," in *International Conference on Learning Representations*, 2021.
- [63] J. Rasley, S. Rajbhandari, O. Ruwase, and Y. He, "Deepspeed: System optimizations enable training deep learning models with over 100 billion parameters," in *Proceedings of the 26th ACM SIGKDD International Conference on Knowledge Discovery & Data Mining*, 2020, pp. 3505–3506.
- [64] A. H. Cano, M. Pagliardini, A. Köpf, K. Matoba, A. Mohtashami, X. Wang *et al.*, "epflm megatron-llm," 2023. [Online]. Available: <https://github.com/epflLLM/Megatron-LLM>
- [65] Z. Luo, C. Xu, P. Zhao, Q. Sun, X. Geng, W. Hu *et al.*, "Wizardcoder: Empowering code large language models with evol-instruct," 2023.
- [66] O. Contributors, "Opencompass: A universal evaluation platform for foundation models," <https://github.com/open-compass/opencompass>, 2023.
- [67] R. Zellers, A. Holtzman, Y. Bisk, A. Farhadi, and Y. Choi, "Hel-laswag: Can a machine really finish your sentence?" *arXiv preprint arXiv:1905.07830*, 2019.
- [68] K. Sakaguchi, R. L. Bras, C. Bhagavatula, and Y. Choi, "Winogrande: An adversarial winograd schema challenge at scale," *Communications of the ACM*, vol. 64, no. 9, pp. 99–106, 2021.
- [69] Y. Bisk, R. Zellers, J. Gao, Y. Choi *et al.*, "Piqa: Reasoning about physical commonsense in natural language," in *Proceedings of the AAAI conference on artificial intelligence*, vol. 34, 2020, pp. 7432–7439.
- [70] P. Clark, I. Cowhey, O. Etzioni, T. Khot, A. Sabharwal, C. Schoenick *et al.*, "Think you have solved question answering? try arc, the ai2 reasoning challenge," *arXiv preprint arXiv:1803.05457*, 2018.
- [71] T. Kwiatkowski, J. Palomaki, O. Redfield, M. Collins, A. Parikh, C. Alberti *et al.*, "Natural questions: a benchmark for question answering research," *Transactions of the Association for Computational Linguistics*, vol. 7, pp. 453–466, 2019.
- [72] M. Joshi, E. Choi, D. S. Weld, and L. Zettlemoyer, "Triviaqa: A large scale distantly supervised challenge dataset for reading comprehension," *arXiv preprint arXiv:1705.03551*, 2017.
- [73] K. Cobbe, V. Kosaraju, M. Bavarian, M. Chen, H. Jun, L. Kaiser *et al.*, "Training verifiers to solve math word problems," *arXiv preprint arXiv:2110.14168*, 2021.
- [74] D. Hendrycks, C. Burns, S. Kadavath, A. Arora, S. Basart, E. Tang *et al.*, "Measuring mathematical problem solving with the math dataset," *arXiv preprint arXiv:2103.03874*, 2021.
- [75] M. Chen, J. Tworek, H. Jun, Q. Yuan, H. P. d. O. Pinto, J. Kaplan *et al.*, "Evaluating large language models trained on code," *arXiv preprint arXiv:2107.03374*, 2021.
- [76] J. Austin, A. Odena, M. Nye, M. Bosma, H. Michalewski, D. Dohan, *et al.*, "Program synthesis with large language models," *arXiv preprint arXiv:2108.07732*, 2021.
- [77] D. Hendrycks, C. Burns, S. Basart, A. Zou, M. Mazeika, D. Song *et al.*, "Measuring massive multitask language understanding," *arXiv preprint arXiv:2009.03300*, 2020.

LoCo: Low-Bit Communication Adaptor for Large-scale Model Training (Supplementary Material)

The appendix supplements the paper titled “Low-Bit Communication Adaptor for Large-scale Model Training” with additional experimental results and technical proofs of convergence. It is structured as follows for ease of navigation and comprehension:

Appendix A provides an introduction to concepts and background knowledge related to distributed training of large-scale models. This section covers sharding strategies for large models and explains operations such as reduce-scatter and all-to-all. These concepts are foundational to understanding the distributed training environment in which LoCo operates.

Appendix B details the specific model configurations and training parameters used in the LLM experiments presented in the main text. Additionally, it includes additional experimental results, offering a more comprehensive view of LoCo’s performance. This section features detailed comparisons of speedup ratios under various settings, models, and training frameworks, providing a deeper insight into the adaptability and efficiency of LoCo.

Appendix C begins by establishing several properties of LoCo, followed by proofs demonstrating the convergence rates of SGD and Adam-type optimizers when combined with the LoCo strategy. These proofs are vital for validating the theoretical underpinnings of LoCo and its effectiveness in optimizing large-scale model training.

Appendix D contains detailed proofs of auxiliary lemmas and properties that support the main arguments and findings in Appendix C.

APPENDIX A PRELIMINARY OF DISTRIBUTED COMMUNICATION

We introduce several concepts relative to the modern distributed communication system in this section

A.1 Scattering and Gathering

All-reduce, reduce-scatter, and all-gather, shown in Fig. 3, are key operations in distributed computing, particularly in the context of LLM training, where they are used to aggregate data like gradients across multiple processors or GPUs.

A.1.1 All-reduce

All-reduce is a collective operation where data from all processors (like gradients from different GPUs) is combined and then redistributed to each processor. This means every processor ends up with the same, fully aggregated result.

A.1.2 Reduce-scatter

Reduce-scatter is the first phase of the all-reduce operation. In this step, each processor contributes its data, which is then partially combined and scattered back to the processors. Thus, each processor ends up with a fragment of the total aggregated data. This process involves sequential data sending, receiving, and reducing operations in a ring-like fashion, ensuring each processor receives a portion of the final aggregated result.

A.1.3 All-gather

All-gather follows reduce-scatter in the all-reduce process. During this phase, each processor shares its fragment of aggregated data with every other processor. By the end of all-gather, all processors have the complete set of aggregated data, vital for further computations. The training process for LLMs utilizing these operations typically unfolds as follows: after the back-propagation phase, a reduce-scatter is employed to distribute and partially aggregate the gradients across the different nodes. Each node then uses these reduced gradients to update its own model weight partition and optimizer’s state. Before the next forward propagation begins, the all-gather operation is utilized to synchronize the weights of the model across all nodes. This ensures that each GPU starts the next iteration of training with the same, updated model parameters. This sequence of operations not only enhances the training efficiency but also ensures consistency and scalability in the distributed training of large-scale models.

A.1.4 Ring-based Reduce-scatter vs. All-to-all

As shown in Fig. 4. The ring-based reduce-scatter operation efficiently divides and distributes data across multiple devices in a ring-like configuration. Each device receives a data chunk, performs a reduction operation (like summing), and passes the reduced data to the next device. This cycle continues until every device has a portion of the aggregated data. The key advantage of this approach is its efficient use of cluster bandwidth and balanced workload distribution among all devices in the ring.

On the other hand, the All-to-all operation, often chosen for its specific benefits like avoiding overflow in certain contexts, involves each process in the cluster sending and receiving unique data segments to and from every other process. It is

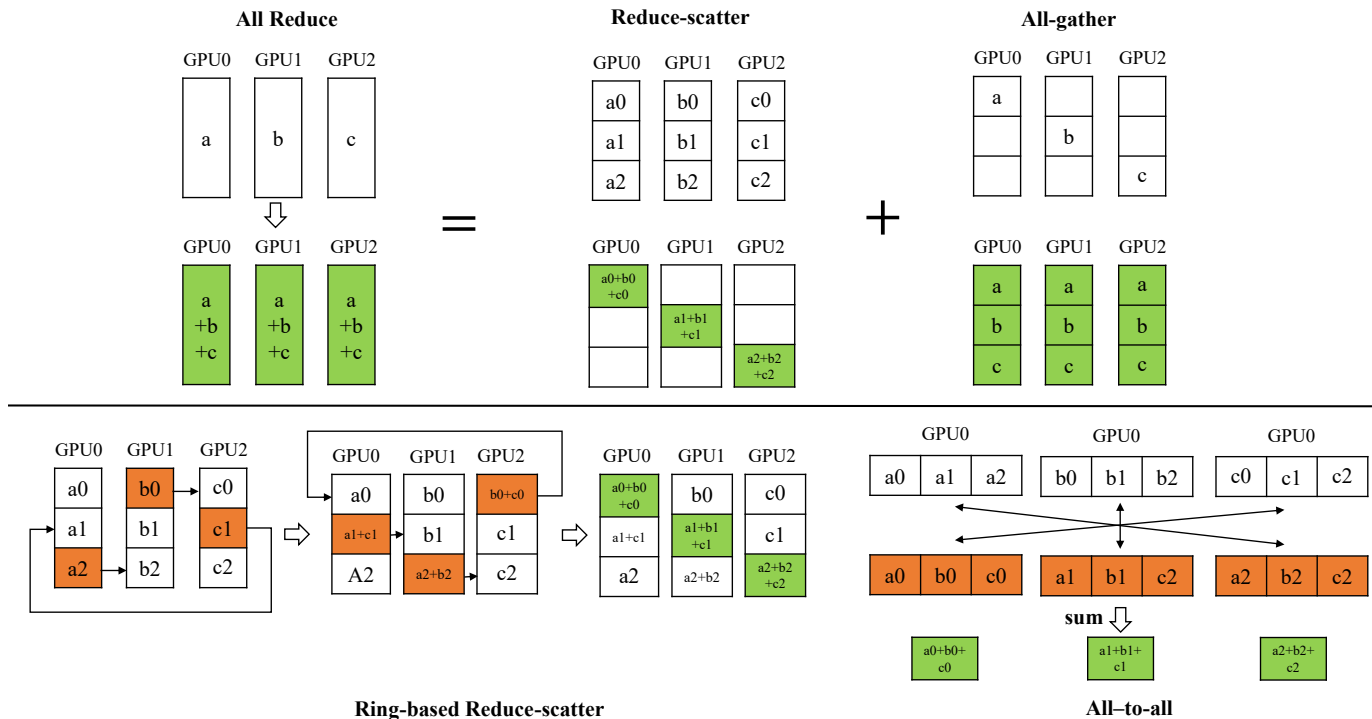


Fig. 3: Overview of All-Reduce and Its Component Operations. The All-Reduce process is depicted in two main phases. Initially, the Reduce-Scatter operations is performed, where gradients are divided and summed up in equal blocks across GPUs according to their ranks. This is followed by the All-Gather phase, where each GPU shares its segment of the aggregated gradients, ensuring the complete set of gradients is available to all GPUs. Additionally, the figure includes representations of the Ring reduce-scatter and Alltoall operations, integral in the gradient distribution and aggregation process across the cluster.

particularly effective in scenarios where each node needs to have a complete picture of the data distributed across the cluster network. The total communication volume in an alltoall operation can be similar to that of a ring-based reduce-scatter when appropriately implemented. This makes alltoall a viable and sometimes preferred choice in certain distributed computing tasks, such as scenarios where overflow avoidance is critical.

A.2 Modern Sharding Strategy

Fully Sharded Data Parallelism (FSDP) revolutionizes the training of deep learning models by optimizing memory usage and computational efficiency across multiple GPUs. As shown in Fig. 4, here is an introduction to FSDP.

A.2.1 Initial Framework without Sharding

Traditionally, in data parallelism without sharding, every GPU holds a complete set of the model's weights, gradients, and optimizer states. The communication between GPUs is limited to performing an all-reduce operation on the entire gradients to facilitate model updates, eliminating the need for sharing other variables. This straightforward communication pattern simplifies operations but comes at the expense of high memory consumption.

A.2.2 Sharded Model

Implementing a sharding strategy significantly enhances memory efficiency. Under this strategy, each GPU maintains only a local partition of the optimizer states, avoiding the need to communicate these states between GPUs. Moreover, each GPU keeps only a partition of the averaged gradients. After backpropagation, non-local portions of the gradients are sent to the respective GPUs via reduce-scatter and subsequently released from memory. This ensures that each GPU updates its segment of the optimizer states and a fraction of the weights. An all-gather operation on the weights follows, maintaining consistency across all GPUs and enabling partial model updates with a reduced memory footprint.

A.2.3 Fully Sharded Data Parallelism

Advancing further, FSDP limits each GPU to holding just a partition of the model weights, eliminating the presence of the complete model on any single GPU. Prior to forward propagation, GPUs collect necessary weight partitions from each other to assemble a full model in memory, conduct forward and backward propagation, and then proceed with gradient reduce-scatter. Post-backpropagation, any non-local weights and gradients are discarded to conserve memory, significantly

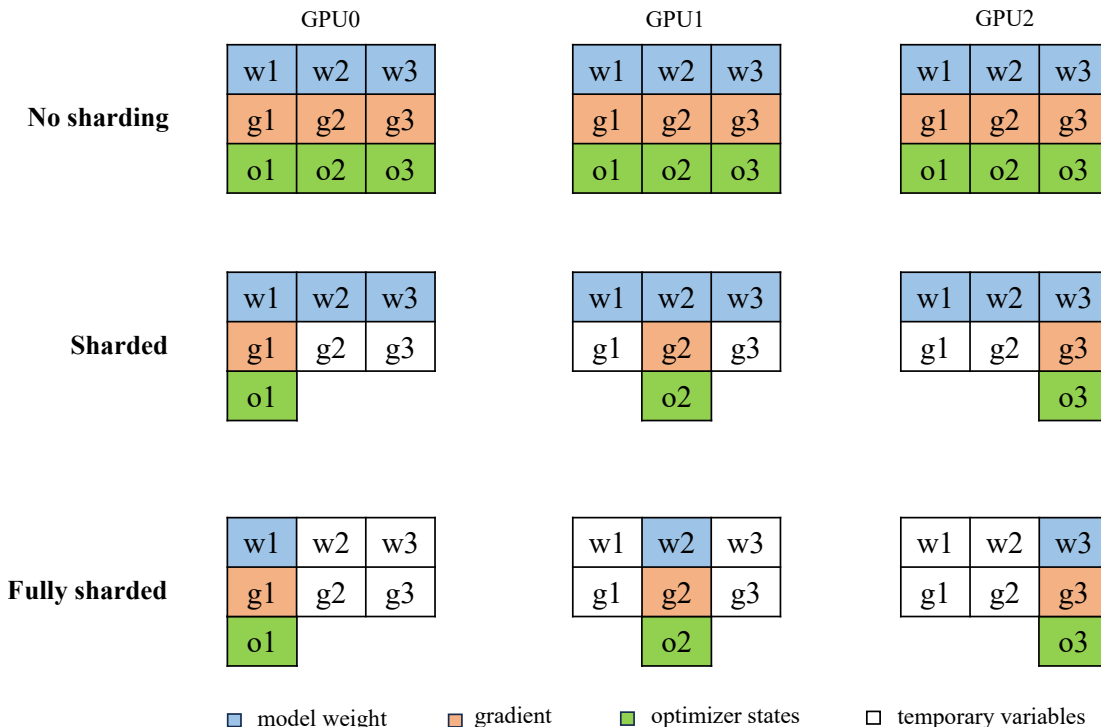


Fig. 4: Overview of sharding strategy. (1) Initial Framework without Sharding, where each GPU stores the entire model, leading to high memory usage but simplified communication; (2) Sharded Model, introducing a strategy where GPUs maintain only local partitions of optimizer states and averaged gradients, enhancing memory efficiency through reduce-scatter and all-gather operations for gradient and weight management; (3) Fully Sharded Data Parallelism, further optimizing memory by limiting each GPU to a partition of the model weights, necessitating inter-GPU collection of weight partitions for model assembly, significantly reducing memory requirements and enabling the training of large-scale models previously constrained by memory limitations.

lowering the memory requirements and fostering complex model training that was previously infeasible due to memory constraints.

While the above explanation outlines the logical framework of FSDP for ease of understanding, it's crucial to acknowledge the sophisticated optimizations embedded within its architecture aimed at further reducing peak memory usage. For more details, please refer to the ZERO strategy [28] and Pytorch FSDP [16]. These include, but are not limited to, layer-wise gradient communication and the strategic release of memory during the backpropagation phase. Such detailed optimizations, though not elaborated here, are fundamental to FSDP's effectiveness in resource management, enabling the scalable and efficient training of large-scale models by adeptly minimizing the peak memory footprint.

APPENDIX B

EXPERIMENTAL DETAILS

B.1 Additional Experimental Results

Here, we present the additional result for the speedup of LoCo on various settings. Firstly, we introduce the concept of accumulation numbers.

Accumulation number: The accumulation number refers to the number of forward and backward passes accumulated before a parameter update occurs in a machine learning model, especially in large-scale training scenarios. In the context of large model training, accumulation number is crucial due to memory constraints and computational efficiency considerations. By accumulating gradients over multiple iterations before updating the model parameters, it's possible to effectively train large models with limited memory resources, especially the large batch size setting. A lower accumulation number leads to a more pronounced speedup in training. This is primarily because a lower accumulation number increases the frequency of communication between nodes. In large-scale training setups, especially with thousands of GPUs, the accumulation number is typically low (e.g., 1 or 2). This low accumulation number significantly magnifies the benefits of methods like LoCo, which reduce communication overhead.

4D parallelism: LoCo's effect is even more pronounced when considering 4D parallel strategies, i.e., data parallelism, pipeline parallelism, tensor parallelism, and expert parallelism. In scenarios where a large number of GPUs are employed, data parallelism often emerges as the simplest and most effective method to increase training parallelism. However, tensor and pipeline parallelism require careful consideration of intra-node and inter-node communications, where the cost of

TABLE 11: Detailed end-to-end speedup of LoCo in prevalent Megatron-LM framework for efficient multi-node LLMs training with different model sizes, gradient accumulation numer, GPU number, and the node connection.

| Model | Accum. Num. | 32× NVIDIA A100 (RoCE v2) | | | 64× NVIDIA A100 (RoCE v2) | | | 128× NVIDIA A100 (RoCE v2) | | |
|--------------|-------------|-----------------------------------|-----------------|--------------|------------------------------|-----------------|--------------|-------------------------------|-----------------|--------------|
| | | Baseline (tokens/s) | LoCo (tokens/s) | Speedup (%) | Baseline (tokens/s) | LoCo (tokens/s) | Speedup (%) | Baseline (tokens/s) | LoCo (tokens/s) | Speedup (%) |
| LLAMA2 (7B) | 4 | 75544.9 | 78911.7 | 4.47 | 148071.9 | 156369.9 | 5.60 | 284840.8 | 307657.4 | 8.01 |
| | 2 | 68330.6 | 73706.1 | 7.87 | 131484.3 | 145277.7 | 10.49 | 254703.8 | 284862.9 | 11.84 |
| | 1 | 57230.2 | 65376.3 | 14.23 | 108680.5 | 127263.1 | 17.10 | 212373.9 | 251701.9 | 18.50 |
| Mistral (7B) | 4 | 74354.6 | 78674.1 | 5.81 | 145855.5 | 154816.9 | 6.14 | 284082.2 | 305136.9 | 7.41 |
| | 2 | 65345.6 | 72734.2 | 11.31 | 128964.8 | 144120.13 | 11.75 | 249414.7 | 281070.5 | 12.69 |
| | 1 | 55947.3 | 64123.7 | 14.61 | 105198.2 | 125422.7 | 19.22 | 206053.7 | 247468.3 | 20.10 |
| LLAMA2 (13B) | 4 | 40341.8 | 43092.1 | 6.82 | 71847.3 | 79106.9 | 10.10 | 139677.0 | 156768.8 | 12.23 |
| | 2 | 35972.6 | 40097.4 | 11.47 | 58235.9 | 69345.9 | 19.07 | 113070.9 | 136932.6 | 21.10 |
| | 1 | 30555.9 | 35683.2 | 16.78 | 43941.6 | 55322.9 | 25.90 | 83160.2 | 108577.2 | 30.56 |
| LLAMA2 (70B) | 4 | | | | 8108.3 | 9870.0 | 21.73 | 15938.6 | 19612.1 | 23.05 |
| | 2 | N/A, since the Data Parallel is 1 | | | 5110.6 | 6503.7 | 27.26 | 9619.7 | 12387.2 | 28.77 |
| | 1 | | | | 2869.2 | 3803.2 | 32.55 | 5263.6 | 7107.6 | 35.03 |
| | Accum. Num. | 32× NVIDIA A800 (Infiniband) | | | 64× NVIDIA A800 (Infiniband) | | | 128× NVIDIA A800 (Infiniband) | | |
| | | Baseline (tokens/s) | LoCo (tokens/s) | Speedup (%) | Baseline (tokens/s) | LoCo (tokens/s) | Speedup (%) | Baseline (tokens/s) | LoCo (tokens/s) | Speedup (%) |
| LLAMA2 (7B) | 4 | 73047.8 | 77834.2 | 6.55 | 136605.5 | 151714.2 | 11.06 | 264459.1 | 295077.9 | 11.58 |
| | 2 | 65542.2 | 73312.9 | 11.86 | 116276.3 | 139874.8 | 20.30 | 216842.1 | 265101.3 | 22.26 |
| | 1 | 54186.8 | 65862.1 | 21.55 | 89555.4 | 120625.6 | 34.69 | 161447.6 | 224887.7 | 39.29 |
| Mistral (7B) | 4 | 71150.4 | 76262.5 | 7.18 | 132480.4 | 147806.4 | 11.57 | 254865.7 | 285780.9 | 12.13 |
| | 2 | 63195.6 | 71579.4 | 13.27 | 111917.1 | 135508.3 | 21.08 | 209780.7 | 258785.6 | 23.36 |
| | 1 | 51896.8 | 63568.5 | 22.49 | 85334.5 | 115355.6 | 35.18 | 155308.7 | 217494.4 | 40.04 |
| LLAMA2 (13B) | 4 | 42515.2 | 46195.4 | 8.65 | 79554.6 | 89581.0 | 12.60 | 151598.8 | 173761.8 | 14.62 |
| | 2 | 37922.1 | 43062.3 | 13.55 | 66455.2 | 81644.0 | 22.86 | 124160.3 | 155571.1 | 25.30 |
| | 1 | 30682.9 | 38226.1 | 24.58 | 49907.4 | 69409.0 | 39.08 | 90446.3 | 128649.6 | 42.24 |

TABLE 12: Speedup achieved by our method against 16-bit communication in PyTorch FSDP framework on MoE model.

| Model | Param. Sharded | Accum. Num. | 32× NVIDIA A800 (Infiniband) | | | 64× NVIDIA A800 (Infiniband) | | |
|----------------|----------------|-------------|------------------------------|-----------------|--------------|------------------------------|-----------------|--------------|
| | | | Baseline (tokens/s) | LoCo (tokens/s) | Speedup (%) | Baseline (tokens/s) | LoCo (tokens/s) | Speedup (%) |
| Mixtral (8×7B) | True | 4 | 76204.6 | 85250.1 | 11.87 | 135825.9 | 148523.5 | 9.35 |
| | | 2 | 34813.2 | 40329.8 | 15.85 | 60963.7 | 71820.3 | 17.81 |
| | | 1 | 14356.1 | 18357.4 | 27.87 | 25450.9 | 34044.7 | 33.77 |

all-reduce operations between nodes can be high. The number of experts available constrains expert parallelism’s efficiency. LoCo greatly reduces communication volumes in the context of data parallelism, accelerating training speed significantly.

Results on training speed: Table 11 and Table 12 show the detailed training speed of LoCo. Notably, there’s a significant improvement in throughput across different models and scales, with larger models seeing more pronounced acceleration. For instance, the 70B LLAMA2 model on the A100 cluster saw a speedup of 23.05% to 35.03%, and the 13B LLAMA2 model on the A800 cluster achieved from 14.62% to 42.24% speedup.

When considering node connections, LoCo demonstrates more substantial improvements in lower bandwidth environments (like the A800 cluster) compared to higher bandwidth scenarios (like the A100 cluster). This suggests that LoCo is particularly effective in optimizing communication efficiency, making it a vital tool in large model training.

Finally, when assessing large-scale training frameworks such as Megatron-LM and PyTorch FSDP, LoCo consistently shows a significant increase in token throughput speed. This highlights its efficacy across different frameworks and training environments, further establishing its utility in large-model training scenarios.

B.2 Model Configurations

The following are the detailed experiment settings for the main parts. All experiments are performed with bfloat-16 precision in default.

GPT-2: Utilizing guidance from Megatron-DeepSpeed¹, as detailed by DeepSpeed [63], we undertook the training of the GPT2-345M model from scratch. Our data source was the OpenWebtext dataset [60], through which we processed a substantial total of 52B tokens. The experiment was configured with a zero optimization stage set to 2, deliberately excluding the use of model and pipeline parallelism to simplify our setup. Our global batch size was set at 512, with a learning rate of $3.0e-4$. In managing the training dynamics, we applied a global gradient norm clipping of 1 and opted for Adam’s optimizer settings with $\beta_1 = 0.9$ and $\beta_2 = 0.95$.

LLAMA2-7B: For LLAMA2-7B, we conduct two experiments on it. **1)** Within the Fully Sharded Data Parallel (FSDP) framework, and following protocols from LLAMA-Accessory [57] and the GPT-4-LLM repository², we conducted a supervised fine-tuning spanning three epochs on the alpaca-gpt4 dataset as per [61]. This process included partitioning both gradient and optimizer states across GPUs, with a global batch size of 64, a learning rate of $2e-5$, gradient clipping at 2, and model parallelism set to 2.

2) Utilizing the Megatron-LM framework [13] and following the methodology of Tiny-LLAMA [56], we performed fine-tuning on the sampled RedPajama dataset³, consuming 8 billion tokens. This setup involved a model parallelism of 8, a total batch size of 1024, and a peak learning rate of $1e-5$, avoiding pipeline parallelism. We matched Adam optimizer’s parameters to those recommended by epfLLM [64], setting $\beta_1 = 0.9$, $\beta_2 = 0.95$, and an ϵ value of $1e-5$, with a maximum token length of 4096 and an ϵ for layer norm also at $1e-5$.

LLAMA2-13B: The fine-tuning of LLAMA2-13B adhered to the identical training hyperparameters as those established for LLAMA2-7B. It’s important to note that we retained most model-related hyperparameters from the Meta’s officially released configurations.

LLAMA2-70B: To accommodate the large-scale model within our memory-constrained training cluster, we made necessary adjustments to the parallelization parameters. Specifically, we set the model parallelism to 8 and the pipeline parallelism to 4, with a max learning rate carefully reduced to $1.5e-4$. All other parameters were consistently aligned with those of the LLAMA2-7B and LLAMA2-13B models.

Mistral-7B: The training configuration for Mistral-7B closely mirrored that of the LLAMA2-7B and LLAMA2-13B models, with the sole exception being a larger maximum learning rate of $5e-5$.

Mixtral 8×7B: Drawing from the LLAMA-Accessory [57], our investigation into the MoE model spanned two experiments, with settings largely coming from LLAMA-Accessory’s demonstrations. We leveraged the FSDP’s checkpointing strategy to alleviate memory demands, setting expert parallelism at 8.

1) For the outcomes presented in Table 2, Mixtral was fine-tuned on the ultrachat-200k dataset [58] over a single epoch. Here, the maximum learning rate was $2.5e-6$, with a global batch size of 128 and a maximum token length of 4096. The Pytorch FSDP sharding strategy was employed to manage gradient and optimizer states efficiently.

2) For the ablation study, we utilized the code-alpaca-v1 dataset [65] for one epoch of fine-tuning, applying a fully sharded strategy to divide gradient, optimizer states, and model weight. Parameters were set with a maximum learning rate of $3e-6$, a global batch size of 128, a maximum token length of 2048, and gradient clipping at 2.

B.3 Benchmarks

Following prior works [26], we conduct downstream evaluation on the popular platform Opencompass [66], and the wide variety of benchmarks used for evaluation are categorized as follows:

- **Commonsense Reasoning (0-shot):** Hellaswag [67], Winogrande [68], PIQA [69], ARC-Easy and ARC-Challenge [70].
- **World Knowledge (5-shot):** NaturalQuestions [71] and TriviaQA [72].
- **Math:** GSM8K (8-shot) [73] and MATH (4-shot) [74].
- **Code:** Humaneval (0-shot) [75] and MBPP (3-shot) [76].
- **Popular aggregated results:** MMLU (5-shot) [77].

1. <https://github.com/microsoft/Megatron-DeepSpeed>

2. <https://github.com/Instruction-Tuning-with-GPT-4/GPT-4-LLM>

3. <https://huggingface.co/datasets/togethercomputer/RedPajama-Data-1T-Sample>

APPENDIX C DETAILED THEORETICAL ANALYSIS

C.1 Auxiliary Lemmas

Lemma 1. For the gradient $\tilde{\mathbf{g}}_k = \frac{1}{N} \sum_{n=1}^N \text{decompressor}(\tilde{\mathbf{h}}_{k+1}^n)$ used to update the parameter in Algorithm 1, we have:

$$\begin{aligned}\tilde{\mathbf{g}}_k &= \frac{1}{N} \sum_{n=1}^N \left(\mathbf{g}_k^n + \frac{1}{\beta} (\tilde{\mathbf{e}}_k^n - \tilde{\mathbf{e}}_{k+1}^n) + \text{decompressor}(\text{compressor}(\tilde{\mathbf{e}}_k^n)) - \tilde{\mathbf{e}}_k^n \right) \\ &= \mathbf{g}_k + \frac{1}{\beta} (\tilde{\mathbf{e}}_k - \tilde{\mathbf{e}}_{k+1}) + \hat{\mathbf{e}}_k - \tilde{\mathbf{e}}_k,\end{aligned}$$

where we let $\mathbf{g}_k := \frac{1}{N} \sum_{n=1}^N \mathbf{g}_k^n$, $\tilde{\mathbf{e}}_k := \frac{1}{N} \sum_{n=1}^N \tilde{\mathbf{e}}_k^n$, $\hat{\mathbf{e}}_k := \frac{1}{N} \sum_{n=1}^N \text{decompressor}(\text{compressor}(\tilde{\mathbf{e}}_k^n))$.

See its proof in Sec. D.1.

Lemma 2. Suppose the setting in Theorem 1 hold, when we use the gradient $\tilde{\mathbf{g}}_k = \frac{1}{N} \sum_{n=1}^N \text{decompressor}(\tilde{\mathbf{h}}_{k+1}^n)$ in Algorithm 1 to update the model weight θ_k in SGD, see Eqn. (9), then we have:

$$\mathbb{E} \left\| \sum_{i=0}^k (\tilde{\mathbf{g}}_i - \mathbf{g}_i) \right\| \leq T_c \sqrt{d} \alpha c_\infty + \frac{\sqrt{dk}}{2s_e},$$

where $\mathbf{g}_k = \frac{1}{N} \sum_{n=1}^N \mathbf{g}_k^n$.

See the proof in Sec. D.2.

Lemma 3. Suppose the setting in Theorem 2 hold, when we use the gradient $\tilde{\mathbf{g}}_k = \frac{1}{N} \sum_{n=1}^N \text{decompressor}(\tilde{\mathbf{h}}_{k+1}^n)$ in Algorithm 1 to update the model weight θ_k in Adam, see Eqn. (9). Considering two sequences $\{\mathbf{m}_k\}_{k=1}^T$:

$$\mathbf{m}_k = (1 - \beta_1) \mathbf{m}_{k-1} + \beta_1 \mathbf{g}_k,$$

and $\{\tilde{\mathbf{m}}_k\}_{k=1}^T$,

$$\tilde{\mathbf{m}}_k = (1 - \beta_1) \tilde{\mathbf{m}}_{k-1} + \beta_1 \tilde{\mathbf{g}}_k,$$

where $\mathbf{g}_k = \frac{1}{N} \sum_{n=1}^N \mathbf{g}_k^n$. Given the sequence of vectors $\{\boldsymbol{\eta}_k\}_{k=0}^T$ such that element-wisely $\boldsymbol{\eta}_k$ satisfy: $\forall i \in [d]$,

$$\eta_{k,i} \leq \eta c_u, \quad |(\eta_{k,i} - \eta_{k-1,i})| \leq \beta_1 \eta c_u, \quad \forall k \in [T],$$

then we have:

$$\mathbb{E} \left\| \sum_{i=0}^k \boldsymbol{\eta}_i \circ (\tilde{\mathbf{m}}_i - \mathbf{m}_i) \right\| \leq (T_c + 1 + \beta_1^2 k T_c) \sqrt{d} \alpha c_\infty c_u \eta + \frac{k \sqrt{d} \eta c_u}{2s_e}.$$

See the proof in Sec. D.3.

Lemma 4. Consider a moving average sequence:

$$\mathbf{m}_k = (1 - \beta) \mathbf{m}_{k-1} + \beta \mathbf{g}_k,$$

where $\mathbf{g}_k = \nabla f(\theta_k) + \boldsymbol{\xi}_k$, and $\boldsymbol{\xi}_k$ is the sample noise such that $\mathbb{E}(\boldsymbol{\xi}_k) = \mathbf{0}$ and $\mathbb{E}\|\boldsymbol{\xi}_k\|^2 \leq \sigma^2$. Then we have:

$$\mathbb{E} \left(\|\mathbf{m}_k - \nabla f(\theta_k)\|^2 \right) \leq (1 - \beta) \mathbb{E} \left(\|\mathbf{m}_{k-1} - \nabla f(\theta_{k-1})\|^2 \right) + \frac{(1 - \beta)^2 L^2}{\beta} \mathbb{E} \left(\|\theta_{k-1} - \theta_k\|^2 \right) + \beta^2 \sigma^2.$$

See the proof in Sec. D.4.

C.2 Convergence Guarantee of LoCo-integrated SGD

We provide the proof of Theorem 1 in this section.

Proof. Consider two sequences $\{\tilde{\theta}_k\}_{k=1}^T$, one is

$$\tilde{\theta}_k = \tilde{\theta}_{k-1} - \eta \tilde{\mathbf{g}}_k = \theta_0 - \eta \sum_{i=0}^k \tilde{\mathbf{g}}_i = \theta_0 - \eta \sum_{i=0}^k \mathbf{g}_i + \eta \left(\sum_{i=0}^k \mathbf{g}_i - \tilde{\mathbf{g}}_i \right),$$

where $\tilde{\mathbf{g}}_k = \frac{1}{N} \sum_{n=1}^N \text{decompressor}(\tilde{\mathbf{h}}_{k+1}^n)$ in Algorithm 1. Another sequence is $\{\theta_k\}_{k=1}^T$:

$$\theta_k = \theta_{k-1} - \eta \mathbf{g}_k = \theta_0 - \eta \sum_{i=0}^k \mathbf{g}_i,$$

where $\mathbf{g}_k := \frac{1}{N} \sum_{n=1}^N \mathbf{g}_k^n = \nabla f(\tilde{\boldsymbol{\theta}}_k) + \boldsymbol{\xi}_k$, and $\boldsymbol{\xi}_k$ is the sample noise such that $\mathbb{E}(\boldsymbol{\xi}_k) = \mathbf{0}$ and $\mathbb{E}\|\boldsymbol{\xi}_k\|^2 \leq \sigma^2$. For and $k \in [T]$, we have:

$$\mathbb{E}\left\|\nabla f(\tilde{\boldsymbol{\theta}}_k) - \nabla f(\boldsymbol{\theta}_k)\right\| \leq L\mathbb{E}\left\|\tilde{\boldsymbol{\theta}}_k - \boldsymbol{\theta}_k\right\| = \eta L\mathbb{E}\left\|\sum_{i=0}^k (\tilde{\mathbf{g}}_i - \mathbf{g}_i)\right\| \leq \eta L\left(T_c\sqrt{d}\alpha c_\infty + \frac{\sqrt{dk}}{2s_e}\right) = \mathcal{O}\left(\eta + \frac{\eta k}{s_e}\right).$$

Since the function f is L -smooth, we can get:

$$\begin{aligned} \mathbb{E}(f(\boldsymbol{\theta}_{k+1})) &\leq \mathbb{E}(f(\boldsymbol{\theta}_k)) + \mathbb{E}\langle \nabla f(\boldsymbol{\theta}_k), \boldsymbol{\theta}_{k+1} - \boldsymbol{\theta}_k \rangle + \frac{L}{2}\|\boldsymbol{\theta}_{k+1} - \boldsymbol{\theta}_k\|^2 \\ &= \mathbb{E}(f(\boldsymbol{\theta}_k)) - \eta \left\langle \nabla f(\boldsymbol{\theta}_k), \nabla f(\tilde{\boldsymbol{\theta}}_k) \right\rangle + \frac{L}{2}\|\boldsymbol{\theta}_{k+1} - \boldsymbol{\theta}_k\|^2 \\ &\leq \mathbb{E}(f(\boldsymbol{\theta}_k)) - \eta \left\|\nabla f(\tilde{\boldsymbol{\theta}}_k)\right\|^2 + \eta \mathbb{E}\left\langle \nabla f(\tilde{\boldsymbol{\theta}}_k) - \nabla f(\boldsymbol{\theta}_k), \nabla f(\tilde{\boldsymbol{\theta}}_k) \right\rangle + \frac{L}{2}\|\boldsymbol{\theta}_{k+1} - \boldsymbol{\theta}_k\|^2 \\ &\leq \mathbb{E}(f(\boldsymbol{\theta}_k)) - \eta \left\|\nabla f(\tilde{\boldsymbol{\theta}}_k)\right\|^2 + \mathcal{O}\left(\eta\left(\eta + \frac{\eta k}{s_e}\right)\sqrt{d}c_\infty\right) + \frac{L\eta^2}{2}\left(\left\|\nabla f(\tilde{\boldsymbol{\theta}}_k)\right\|^2 + \frac{\sigma^2}{N}\right). \end{aligned}$$

By setting $\eta \leq \frac{1}{L}$, we have:

$$\frac{1}{T} \sum_{k=0}^T \mathbb{E}\left\|\nabla f(\tilde{\boldsymbol{\theta}}_k)\right\|^2 \leq \frac{2(f(\tilde{\boldsymbol{\theta}}_0) - f(\tilde{\boldsymbol{\theta}}^*))}{\eta T} + \mathcal{O}(\eta\sqrt{d}c_\infty) + \mathcal{O}\left(\frac{\eta T\sqrt{d}c_\infty}{s_e}\right) + \mathcal{O}\left(\frac{\eta L\sigma^2}{N}\right).$$

where $\tilde{\boldsymbol{\theta}}^* \in \arg\min_{\boldsymbol{\theta}} f(\boldsymbol{\theta})$. By setting $\eta = \mathcal{O}(\epsilon^2)$, $T = \mathcal{O}(\epsilon^{-4})$, and $s_e = \Omega(\epsilon^{-4})$, we have:

$$\frac{1}{T} \sum_{k=0}^T \mathbb{E}\left\|\nabla f(\tilde{\boldsymbol{\theta}}_k)\right\|^2 \leq \mathcal{O}\left(\epsilon^2\left(\left(f(\tilde{\boldsymbol{\theta}}_0) - f(\tilde{\boldsymbol{\theta}}^*)\right) + \sqrt{d}c_\infty + \frac{L\sigma^2}{N}\right)\right) = \mathcal{O}(\epsilon^2).$$

We finish the proof on SGD. □

C.3 Convergence Guarantee of LoCo-integrated Adam-family Optimizers

We provide the proof of Theorem 2 in this section.

Proof. Similar to the proof of Theorem 1 in Sec.C.2, we also consider two sequences $\{\boldsymbol{\theta}_k\}_{k=1}^T$:

$$\boldsymbol{\theta}_k = \boldsymbol{\theta}_{k-1} - \boldsymbol{\eta}_k \circ \mathbf{m}_k = \boldsymbol{\theta}_0 - \sum_{i=0}^k \boldsymbol{\eta}_i \circ \mathbf{m}_i, \quad \text{where } \mathbf{m}_k = (1 - \beta_1)\mathbf{m}_{k-1} + \beta_1\mathbf{g}_k,$$

and $\{\tilde{\boldsymbol{\theta}}_k\}_{k=1}^T$,

$$\tilde{\boldsymbol{\theta}}_k = \tilde{\boldsymbol{\theta}}_{k-1} - \boldsymbol{\eta}_k \circ \tilde{\mathbf{m}}_k = \boldsymbol{\theta}_0 - \sum_{i=0}^k \boldsymbol{\eta}_i \circ \tilde{\mathbf{m}}_i = \boldsymbol{\theta}_0 - \sum_{i=0}^k \boldsymbol{\eta}_i \circ \mathbf{m}_i + \left(\sum_{i=0}^k \boldsymbol{\eta}_i \circ (\mathbf{m}_i - \tilde{\mathbf{m}}_i)\right),$$

where,

$$\tilde{\mathbf{m}}_k = (1 - \beta_1)\tilde{\mathbf{m}}_{k-1} + \beta_1\tilde{\mathbf{g}}_k.$$

From Lemma 4, for and $k \in [T]$, we have:

$$\mathbb{E}\left\|\sum_{i=0}^k \boldsymbol{\eta}_i \circ (\tilde{\mathbf{m}}_i - \mathbf{m}_i)\right\| \leq (T_c + 1 + \beta_1^2 k T_c)\sqrt{d}\alpha c_\infty c_u \eta + \frac{k\sqrt{d}\eta c_u}{2s_e} \leq 2T_c\sqrt{d}\alpha c_\infty c_u \eta + \frac{k\sqrt{d}\eta c_u}{2s_e},$$

where the last inequality we use the assumption $\beta_1 = \mathcal{O}(\epsilon^2)$ and $k \leq T = \Omega(\epsilon^{-4})$. Then, we can get the following:

$$\mathbb{E}\left\|\nabla f(\tilde{\boldsymbol{\theta}}_k) - \nabla f(\boldsymbol{\theta}_k)\right\| \leq L\mathbb{E}\left\|\sum_{i=0}^k \boldsymbol{\eta}_i \circ (\tilde{\mathbf{m}}_i - \mathbf{m}_i)\right\| \leq 2LT_c\sqrt{d}\alpha c_\infty c_u \eta + \frac{kL\sqrt{d}\eta c_u}{2s_e}. \quad (12)$$

We also get the following:

$$\mathbb{E}\left\|\tilde{\boldsymbol{\theta}}_k - \boldsymbol{\theta}_k\right\|^2 \leq \mathbb{E}\left\|\sum_{i=0}^k \boldsymbol{\eta}_i \circ (\tilde{\mathbf{m}}_i - \mathbf{m}_i)\right\|^2 \leq 8T_c^2 d\alpha^2 c_\infty^2 c_u^2 \eta^2 + \frac{k^2 d c_u^2 \eta^2}{2s_e^2}. \quad (13)$$

For convenience, we let:

$$c_a := 8T_c^2 d\alpha^2 c_\infty^2 c_u^2, \quad c_b := \frac{d c_u^2}{2}, \quad c_e := 2LT_c d\alpha c_\infty^2 c_u^2, \quad c_d := \frac{Ld c_\infty c_u^2}{2}.$$

Based on the L -smoothness of $f(\cdot)$, we have:

$$\begin{aligned}
& \mathbb{E}(f(\boldsymbol{\theta}_{k+1})) \leq \mathbb{E}(f(\boldsymbol{\theta}_k)) + \mathbb{E}\langle \nabla f(\boldsymbol{\theta}_k), \boldsymbol{\theta}_{k+1} - \boldsymbol{\theta}_k \rangle + \frac{L}{2} \mathbb{E} \|\boldsymbol{\theta}_{k+1} - \boldsymbol{\theta}_k\|^2 \\
& = \mathbb{E}(f(\boldsymbol{\theta}_k)) - \mathbb{E} \langle \nabla f(\boldsymbol{\theta}_k), \boldsymbol{\eta}_k \circ \mathbf{m}_k \rangle + \frac{L}{2} \mathbb{E} \|\boldsymbol{\eta}_k \circ \mathbf{m}_k\|^2 \\
& = \mathbb{E}(f(\boldsymbol{\theta}_k)) - \mathbb{E} \langle \nabla f(\tilde{\boldsymbol{\theta}}_k), \boldsymbol{\eta}_k \circ \mathbf{m}_k \rangle + \frac{L}{2} \mathbb{E} \|\boldsymbol{\eta}_k \circ \mathbf{m}_k\|^2 + \mathbb{E} \langle \nabla f(\tilde{\boldsymbol{\theta}}_k) - \nabla f(\boldsymbol{\theta}_k), \boldsymbol{\eta}_k \circ \mathbf{m}_k \rangle \\
& \stackrel{\textcircled{1}}{\leq} \mathbb{E}(f(\boldsymbol{\theta}_k)) - \mathbb{E} \langle \nabla f(\tilde{\boldsymbol{\theta}}_k), \boldsymbol{\eta}_k \circ \mathbf{m}_k \rangle + \frac{L}{2} \mathbb{E} \|\boldsymbol{\eta}_k \circ \mathbf{m}_k\|^2 + \left(c_e \eta^2 + \frac{c_d \eta^2 k}{s_e} \right) \\
& = \mathbb{E}(f(\boldsymbol{\theta}_k)) + \frac{1}{2} \mathbb{E} \left\| \sqrt{\boldsymbol{\eta}_k} \circ (\nabla f(\tilde{\boldsymbol{\theta}}_k) - \mathbf{m}_k) \right\|^2 - \frac{1}{2} \mathbb{E} \left\| \sqrt{\boldsymbol{\eta}_k} \circ \nabla f(\tilde{\boldsymbol{\theta}}_k) \right\|^2 - \frac{1}{2} \mathbb{E} \|\sqrt{\boldsymbol{\eta}_k} \circ \mathbf{m}_k\|^2 \\
& \quad + \frac{L}{2} \mathbb{E} \|\boldsymbol{\eta}_k \circ \mathbf{m}_k\|^2 + \left(c_e \eta^2 + \frac{c_d \eta^2 k}{s_e} \right) \\
& \stackrel{\textcircled{2}}{\leq} \mathbb{E}(f(\boldsymbol{\theta}_k)) + \frac{\eta c_u}{2} \mathbb{E} \left\| \nabla f(\tilde{\boldsymbol{\theta}}_k) - \mathbf{m}_k \right\|^2 - \frac{\eta c_l}{2} \mathbb{E} \left\| f(\tilde{\boldsymbol{\theta}}_k) \right\|^2 + \left(\frac{L \eta^2 c_u^2}{2} - \frac{\eta c_l}{2} \right) \mathbb{E} \|\mathbf{m}_k\|^2 + \left(c_e \eta^2 + \frac{c_d \eta^2 k}{s_e} \right) \\
& \stackrel{\textcircled{3}}{\leq} \mathbb{E}(f(\boldsymbol{\theta}_k)) + \frac{\eta c_u}{2} \mathbb{E} \left\| \nabla f(\tilde{\boldsymbol{\theta}}_k) - \mathbf{m}_k \right\|^2 - \frac{\eta c_l}{2} \mathbb{E} \left\| f(\tilde{\boldsymbol{\theta}}_k) \right\|^2 - \frac{\eta c_l}{4} \mathbb{E} \|\mathbf{m}_k\|^2 + \left(c_e \eta^2 + \frac{c_d \eta^2 k}{s_e} \right),
\end{aligned} \tag{14}$$

where $\textcircled{1}$ is due to Eqn. (12), $\textcircled{2}$ comes from the boundness of $\boldsymbol{\eta}_k$, and in $\textcircled{3}$ we set $\eta \leq \frac{c_l}{2Lc_u^2}$ so that $\frac{L\eta^2 c_u^2}{2} \leq \frac{\eta c_l}{4}$.

Then from Lemma 4, we already have:

$$\begin{aligned}
& \mathbb{E} \left(\left\| \mathbf{m}_k - \nabla f(\tilde{\boldsymbol{\theta}}_k) \right\| \right) \leq (1 - \beta_1) \mathbb{E} \left\| \mathbf{m}_{k-1} - \nabla f(\tilde{\boldsymbol{\theta}}_{k-1}) \right\| + \frac{(1 - \beta_1)^2 L^2}{\beta_1} \mathbb{E} \left\| \tilde{\boldsymbol{\theta}}_{k-1} - \tilde{\boldsymbol{\theta}}_k \right\|^2 + \frac{\beta_1^2 \sigma^2}{N} \\
& \stackrel{\textcircled{1}}{\leq} (1 - \beta_1) \mathbb{E} \left\| \mathbf{m}_{k-1} - \nabla f(\tilde{\boldsymbol{\theta}}_{k-1}) \right\| + \frac{3\eta^2 c_u^2 (1 - \beta_1)^2 L^2}{\beta_1} \mathbb{E} \|\mathbf{m}_{k-1}\|^2 + \frac{\beta_1^2 \sigma^2}{N} + 3 \left(c_a \eta^2 + \frac{c_b \eta^2 k^2}{s_e^2} \right),
\end{aligned} \tag{15}$$

where $\textcircled{1}$ holds since we have: $\boldsymbol{\theta}_{k-1} - \boldsymbol{\theta}_k = \boldsymbol{\eta}_{k-1} \circ \mathbf{m}_{k-1}$,

$$\mathbb{E} \left\| \tilde{\boldsymbol{\theta}}_{k-1} - \tilde{\boldsymbol{\theta}}_k \right\|^2 \leq 3 \left(\mathbb{E} \|\boldsymbol{\theta}_{k-1} - \boldsymbol{\theta}_k\|^2 + \mathbb{E} \left\| \tilde{\boldsymbol{\theta}}_k - \boldsymbol{\theta}_k \right\|^2 + \mathbb{E} \left\| \boldsymbol{\theta}_{k-1} - \tilde{\boldsymbol{\theta}}_{k-1} \right\|^2 \right).$$

Next, we add Eqn. (14) and $a \times$ Eqn. (15), and obtain:

$$\begin{aligned}
& \mathbb{E}(f(\boldsymbol{\theta}_{k+1})) + a \mathbb{E} \|\mathbf{m}_{k+1} - \nabla f(\tilde{\boldsymbol{\theta}}_{k+1})\|^2 \\
& \leq \mathbb{E}(f(\boldsymbol{\theta}_k)) + \left(\frac{\eta c_u}{2} + a(1 - \beta_1) \right) \mathbb{E} \left\| \nabla f(\tilde{\boldsymbol{\theta}}_k) - \mathbf{m}_k \right\|^2 - \frac{\eta c_l}{2} \mathbb{E} \left\| \nabla f(\tilde{\boldsymbol{\theta}}_k) \right\|^2 \\
& \quad - \left(\frac{\eta c_l}{4} - \frac{3a\eta^2 c_u^2 (1 - \beta_1)^2 L^2}{\beta_1} \right) \mathbb{E} \|\mathbf{m}_k\|^2 + \frac{a\beta_1^2 \sigma^2}{N} + \left(c_e \eta^2 + \frac{c_d \eta^2 k}{s_e} + 3a \left(c_a \eta^2 + \frac{c_b \eta^2 k^2}{s_e^2} \right) \right).
\end{aligned}$$

Let $a = \frac{\eta c_u}{\beta_1}$ and $G(\boldsymbol{\theta}_k) = \mathbb{E}(f(\boldsymbol{\theta}_k)) + \frac{\eta c_u}{\beta_1} \mathbb{E} \left\| \nabla f(\tilde{\boldsymbol{\theta}}_k) - \mathbf{m}_k \right\|^2$. Then we have:

$$\begin{aligned}
G(\boldsymbol{\theta}_{k+1}) & \leq G(\boldsymbol{\theta}_k) - \frac{\eta c_l}{2} \mathbb{E} \left\| \nabla f(\tilde{\boldsymbol{\theta}}_k) \right\|^2 - \left(\frac{\eta c_l}{4} - \frac{3\eta^3 c_u^3 (1 - \beta_1)^2 L^2}{\beta_1^2} \right) \mathbb{E} \|\mathbf{m}_k\|^2 \\
& \quad + \frac{\eta \beta_1 c_u \sigma^2}{N} + \left(c_e \eta^2 + \frac{c_d \eta^2 k}{s_e} + \frac{3c_a c_u \eta^3}{\beta_1} + \frac{3c_u c_b \eta^3 k^2}{\beta_1 s_e^2} \right) \\
& \stackrel{\textcircled{1}}{\leq} G(\boldsymbol{\theta}_k) - \frac{\eta c_l}{2} \mathbb{E} \left\| \nabla f(\tilde{\boldsymbol{\theta}}_k) \right\|^2 - \frac{\eta c_l}{8} \mathbb{E} \|\mathbf{m}_k\|^2 \\
& \quad + \frac{\eta \beta_1 c_u \sigma^2}{N} + \left(c_e \eta^2 + \frac{c_d \eta^2 k}{s_e} + \frac{3c_a c_u \eta^3}{\beta_1} + \frac{3c_u c_b \eta^3 k^2}{\beta_1 s_e^2} \right),
\end{aligned}$$

where $\textcircled{1}$ is due to the setting $\eta \leq \frac{\beta_1 c_l^{0.5}}{5c_u^{1.5}(1-\beta_1)L}$.

Next, we can sum the above inequality from $k = 0$ to $k = T - 1$, and obtain:

$$\begin{aligned}
\frac{1}{T} \sum_{k=0}^{T-1} \mathbb{E} \left[\left\| \nabla f(\tilde{\boldsymbol{\theta}}_k) \right\|^2 + \frac{1}{4} \|\mathbf{m}_k\|^2 \right] & \leq \frac{2(G(\boldsymbol{\theta}_0) - G(\boldsymbol{\theta}_{T-1}))}{c_l \eta T} + \frac{2\beta_1 c_u \sigma^2}{c_l N} + \left(\frac{2c_e \eta}{c_l} + \frac{2c_d \eta k}{c_l s_e} + \frac{6c_a c_u \eta^2}{c_l \beta_1} + \frac{6c_u c_b \eta^2 T^2}{c_l \beta_1 s_e^2} \right) \\
& \stackrel{\textcircled{1}}{\leq} \frac{2\Delta}{c_l \eta T} + \frac{2c_u \sigma^2}{c_l \beta_1 N T} + \frac{2\beta_1 c_u \sigma^2}{c_l N} + \left(\frac{2c_e \eta}{c_l} + \frac{2c_d \eta k}{c_l s_e} + \frac{6c_a c_u \eta^2}{c_l \beta_1} + \frac{6c_u c_b \eta^2 T^2}{c_l \beta_1 s_e^2} \right),
\end{aligned}$$

where ① comes from:

$$\begin{aligned} G(\boldsymbol{\theta}_0) - G(\boldsymbol{\theta}_{T-1}) &= \mathbb{E}(f(\boldsymbol{\theta}_0)) + \frac{\eta c_u}{\beta_1} \mathbb{E} \|\nabla f(\boldsymbol{\theta}_0) - \mathbf{m}_0\|^2 - \mathbb{E}(f(\boldsymbol{\theta}_{T-1})) - \frac{\eta c_u}{\beta_1} \mathbb{E} \left\| \nabla f(\tilde{\boldsymbol{\theta}}_{T-1}) - \mathbf{m}_{T-1} \right\|^2 \\ &\leq \mathbb{E}(f(\boldsymbol{\theta}_0)) + \frac{\eta c_u}{\beta_1} \mathbb{E} \|\nabla f(\boldsymbol{\theta}_0) - \mathbf{m}_0\|^2 - \mathbb{E}(f(\boldsymbol{\theta}_{T-1})) \\ &\leq \Delta + \frac{\eta c_u \sigma^2}{\beta_1 N}, \end{aligned}$$

where $\Delta := \mathbb{E}(f(\boldsymbol{\theta}_0)) - \mathbb{E}(f(\boldsymbol{\theta}_*)) \geq \mathbb{E}(f(\boldsymbol{\theta}_0)) - \mathbb{E}(f(\boldsymbol{\theta}_{T-1}))$.

By setting $T = \Omega(\epsilon^{-4})$, $\beta_1 = \mathcal{O}(\epsilon^2)$, $\eta = \mathcal{O}(\epsilon^2)$ and $s_e = \Omega(\epsilon^{-4})$, we have

$$\frac{1}{T} \sum_{k=0}^{T-1} \mathbb{E} \left[\|\nabla f(\boldsymbol{\theta}_k)\|^2 + \frac{1}{4} \|\mathbf{m}_k\|^2 \right] \leq \epsilon^2.$$

The proof is completed. \square

APPENDIX D PROOFS OF AUXILIARY LEMMAS

Before providing the formal proofs for the auxiliary lemmas, we provide two foundation lemmas.

Lemma 5. *Give the bit length p and the scalar $s > 0$, consider the following operator: $\forall x > 0$,*

$$\mathcal{C}(x) := \frac{\text{float}(\text{round}_{p\text{-bit}}(x \times s))}{s}.$$

We have the following properties:

$$|\mathcal{C}(x)| \leq \frac{2^{p+1} + 1}{2s}, \quad |x - \mathcal{C}(x)| \leq \begin{cases} \frac{1}{2s}, & \text{if } |x| \leq \frac{2^p}{s}, \\ |x| - \frac{2^p}{s}, & \text{if } |x| > \frac{2^p}{s}, \end{cases} \quad |x - \mathcal{C}(x)| \leq 2|x|.$$

Proof. When $|x| \leq \frac{2^p}{s}$, according to the properties of rational numbers, there are two integers n_k and n_{k+1} such that:

$$\frac{n_k}{s} \leq x \leq \frac{n_{k+1}}{s}.$$

According to the definition of the operator $\mathcal{C}(\cdot)$, we have:

$$\mathcal{C}(x) = \begin{cases} \frac{n_k}{s}, & \text{if } x \leq \frac{2n_k+1}{2s}, \\ \frac{n_{k+1}}{s}, & \text{else.} \end{cases} \quad (16)$$

Hence, when $|x| \leq \frac{2^p}{s}$, we conclude that $|x - \mathcal{C}(x)| \leq \frac{1}{2s} \leq 2|x|$. Considering the case $|x| > \frac{2^p}{s}$, we can easily find that $\mathcal{C}(x) = \text{sgn}(x) \frac{s^p}{s}$, where sgn is the sign function. Thus, we have $|x - \mathcal{C}(x)| = |x| - \frac{2^p}{s}$. Then, we can conclude that:

$$|x - \mathcal{C}(x)| \leq \begin{cases} \frac{1}{2s}, & \text{if } |x| \leq \frac{2^p}{s}, \\ |x| - \frac{2^p}{s}, & \text{if } |x| > \frac{2^p}{s}, \end{cases} \quad |x - \mathcal{C}(x)| \leq 2|x|.$$

On the other hand, we could verify that, $|\mathcal{C}(x)| = \frac{2^p}{s}$ when $|x| > \frac{2^p}{s}$. By Eqn. (16), we have $|\mathcal{C}(x)| \leq |x| + \frac{1}{2s}$ when $|x| \leq \frac{2^p}{s}$. Thus, we have:

$$|\mathcal{C}(x)| \leq \frac{2^p}{s} + \frac{1}{2s} = \frac{2^{p+1} + 1}{2s}.$$

We finish the proof. \square

Lemma 6. *We can get the bound of $\mathbb{E}\|\tilde{\mathbf{e}}_k^n\|$:*

$$\mathbb{E}\|\tilde{\mathbf{e}}_k^n\| \leq T_c \sqrt{d} \alpha \beta c_\infty.$$

We let $\tilde{\mathbf{e}}_k := \frac{1}{N} \sum_{n=1}^N \tilde{\mathbf{e}}_k^n$, which further yields:

$$\mathbb{E}\|\tilde{\mathbf{e}}_k\| = \mathbb{E} \left\| \frac{1}{N} \sum_{n=1}^N \tilde{\mathbf{e}}_k^n \right\| \leq \frac{1}{N} \sum_{n=1}^N \mathbb{E}\|\tilde{\mathbf{e}}_k^n\| \leq T_c \sqrt{d} \alpha \beta c_\infty. \quad (17)$$

Proof. For convenience, we denote that:

$$\mathcal{C}_c(\cdot) := \text{decompressor} \circ \text{compressor}(\cdot, s, p), \quad \mathcal{C}_d(\cdot) := \text{decompressor} \circ \text{compressor}(\cdot, s_e, p_e), \quad k' := k - \lfloor k/T_c \rfloor \times T_c.$$

We prove the results by induction on the i -th element of the vector $\tilde{\mathbf{e}}_k^n$. We first try to prove that $|\tilde{e}_{k,i}^n| \leq k' \alpha \beta c_\infty$. Since we reset the error vector periodically, i.e., $\tilde{\mathbf{e}}_k^n = \mathbf{0}$ when $k' = 0$, only the case of $k' = 1$ to $k' = T_c - 1$ needs to be considered. Note that, for the i -th element of the vector $\tilde{\mathbf{e}}_k^n$, we have:

$$|\tilde{e}_{k,i}^n| \leq (1 - \beta) |\tilde{e}_{k-1,i}^n| + \beta |h_{k-1,i}^n - \mathcal{C}_c(h_{k-1,i}^n)|.$$

For $k' = 1$, i.e., just after the resetting, we consider two cases. If $|h_{k-1,i}^n| \leq \frac{2^p}{s}$, then:

$$|\tilde{e}_{k,i}^n| \leq \frac{\beta}{2s}.$$

If $|h_{k-1,i}^n| > \frac{2^p}{s}$, we have:

$$|\tilde{e}_{k,i}^n| \leq \beta |h_{k-1,i}^n - \mathcal{C}_c(h_{k-1,i}^n)| \leq \beta \left(|h_{k-1,i}^n| - \frac{2^p}{s} \right) \leq \beta \left(|g_{k-1,i}^n| - \frac{2^p}{s} \right) \leq \alpha \beta c_\infty,$$

where the last inequality comes from the assumption $\frac{2^p}{s(1-\alpha)} \geq c_\infty$. Hence, we can conclude that $|\tilde{e}_{k,i}^n| \leq k' \alpha \beta c_\infty$ for $k' = 1$, i.e., the first error vector during this reset period holds the bounds. Now, we assume that for all $(\lfloor k/T_c \rfloor \times T_c) \leq t < k$ hold the bounds $|\tilde{e}_{t,i}^n| \leq t' \alpha \beta c_\infty$. Then we consider the case for $\tilde{e}_{k,i}^n$. If $|h_{k-1,i}^n| \leq \frac{2^p}{s}$, then:

$$|\tilde{e}_{k,i}^n| \leq (1 - \beta) |\tilde{e}_{k-1,i}^n| + \frac{\beta}{2s}.$$

If $|h_{k-1,i}^n| > \frac{2^p}{s}$, we have:

$$\begin{aligned} |\tilde{e}_{k,i}^n| &\leq (1 - \beta) |\tilde{e}_{k-1,i}^n| + \beta |h_{k-1,i}^n - \mathcal{C}_c(h_{k-1,i}^n)| \leq (1 - \beta) |\tilde{e}_{k-1,i}^n| + \beta \left(|h_{k-1,i}^n| - \frac{2^p}{s} \right) \\ &\leq (1 - \beta) |\tilde{e}_{k-1,i}^n| + \beta \left(|g_{k-1,i}^n| + |\tilde{e}_{k-1,i}^n| + |\tilde{e}_{k-1,i}^n - \mathcal{C}_d(\tilde{e}_{k-1,i}^n)| - \frac{2^p}{s} \right) \\ &\leq |\tilde{e}_{k-1,i}^n| + \alpha \beta c_\infty. \end{aligned}$$

where the last inequality comes from the assumption $\frac{2^p}{s} \geq (1 - \alpha)c_\infty + \frac{1}{2s_e}$ and $T_c \alpha \beta s_e c_\infty \leq 2^{p_e}$. Combing all the cases together, we get:

$$|\tilde{e}_{k,i}^n| \leq |\tilde{e}_{k-1,i}^n| + \alpha \beta c_\infty \leq |\tilde{e}_{k-2,i}^n| + 2\alpha \beta c_\infty \leq k' \alpha \beta c_\infty.$$

Then, the conclusion is obvious since $k' \leq T_c$. □

D.1 Proof of Lemma 1

Proof. For the gradient $\bar{\mathbf{g}}_k$, it is defined as:

$$\begin{aligned} \bar{\mathbf{g}}_k &= \frac{1}{N} \sum_{n=1}^N \text{decompressor}(\tilde{\mathbf{h}}_{k+1}^n) = \frac{1}{N} \sum_{n=1}^N \text{decompressor}(\text{compressor}(\mathbf{h}_{k+1}^n)) \\ &= \frac{1}{N} \sum_{n=1}^N \mathbf{h}_{k+1}^n + \text{decompressor}(\text{compressor}(\mathbf{h}_{k+1}^n)) - \mathbf{h}_{k+1}^n \\ &\stackrel{\textcircled{1}}{=} \frac{1}{N} \sum_{n=1}^N \mathbf{g}_k^n + \text{decompressor}(\mathbf{e}_k^n) + \text{decompressor}(\text{decompressor}(\mathbf{h}_{k+1}^n)) - \mathbf{h}_{k+1}^n \\ &\stackrel{\textcircled{2}}{=} \frac{1}{N} \sum_{n=1}^N \mathbf{g}_k^n + \text{decompressor}(\mathbf{e}_{k+1}^n) - \boldsymbol{\delta}_{k+1}^n, \end{aligned}$$

where $\textcircled{1}$ uses $\mathbf{h}_{k+1}^n = \mathbf{g}_k^n + \text{decompressor}(\mathbf{e}_k^n)$, and in $\textcircled{2}$, we define:

$$\boldsymbol{\delta}_k^n := \mathbf{h}_k^n - \text{decompressor}(\text{compressor}(\mathbf{h}_k^n)).$$

At the same time, we have

$$\begin{aligned} \text{decompressor}(\mathbf{e}_k^n) - \boldsymbol{\delta}_{k+1}^n &\stackrel{\textcircled{1}}{=} \text{decompressor}(\mathbf{e}_k^n) - \frac{1}{\beta} (\tilde{\mathbf{e}}_{k+1}^n - (1 - \beta)\tilde{\mathbf{e}}_k^n) \\ &= \text{decompressor}(\text{compressor}(\tilde{\mathbf{e}}_k^n)) - \frac{1}{\beta} (\tilde{\mathbf{e}}_{k+1}^n - (1 - \beta)\tilde{\mathbf{e}}_k^n) \\ &= \frac{1}{\beta} (\tilde{\mathbf{e}}_k^n - \tilde{\mathbf{e}}_{k+1}^n) + \text{decompressor}(\text{compressor}(\tilde{\mathbf{e}}_k^n)) - \tilde{\mathbf{e}}_k^n, \end{aligned}$$

where in ① we use $\delta_k^n = \frac{1}{\beta} (\tilde{\mathbf{e}}_k^n - (1 - \beta)\tilde{\mathbf{e}}_{k-1}^n)$ from the Algorithm. Accordingly, we have:

$$\bar{\mathbf{g}}_k = \frac{1}{N} \sum_{n=1}^N \left(\mathbf{g}_k^n + \frac{1}{\beta} (\tilde{\mathbf{e}}_k^n - \tilde{\mathbf{e}}_{k+1}^n) + \text{decompressor}(\text{compressor}(\tilde{\mathbf{e}}_k^n)) - \tilde{\mathbf{e}}_k^n \right).$$

We complete the proof. \square

D.2 Proof of Lemma 2

Proof. In Lemma 1, we already have: $\bar{\mathbf{g}}_k = \mathbf{g}_k + \frac{1}{\beta} (\tilde{\mathbf{e}}_k - \tilde{\mathbf{e}}_{k+1}) + \hat{\mathbf{e}}_k - \tilde{\mathbf{e}}_k$, where we let $\mathbf{g}_k := \frac{1}{N} \sum_{n=1}^N \mathbf{g}_k^n$, $\tilde{\mathbf{e}}_k := \frac{1}{N} \sum_{n=1}^N \tilde{\mathbf{e}}_k^n$, and $\hat{\mathbf{e}}_k := \frac{1}{N} \sum_{n=1}^N \mathcal{C}_d(\tilde{\mathbf{e}}_k^n)$. In this way, by the results from Lemma 6, we can bound:

$$\begin{aligned} \mathbb{E} \left\| \sum_{i=0}^k (\bar{\mathbf{g}}_i - \mathbf{g}_i) \right\| &= \mathbb{E} \left\| \frac{1}{\beta} \sum_{i=0}^k ((\tilde{\mathbf{e}}_i - \tilde{\mathbf{e}}_{i+1}) + \hat{\mathbf{e}}_i - \tilde{\mathbf{e}}_i) \right\| \leq \frac{1}{\beta} \mathbb{E} \|\tilde{\mathbf{e}}_k\| + \frac{1}{N} \mathbb{E} \left\| \sum_{n=1, i=1}^{N, k} \tilde{\mathbf{e}}_i^n - \mathcal{C}_d(\tilde{\mathbf{e}}_i^n) \right\| \\ &\stackrel{\textcircled{1}}{\leq} \frac{T_c \sqrt{d} \alpha \beta c_\infty}{\beta} + \frac{1}{N} \frac{\sqrt{d} N k}{2s_e} = T_c \sqrt{d} \alpha c_\infty + \frac{\sqrt{d} k}{2s_e}, \end{aligned}$$

where ① comes from Eqn. (17), and the assumption that $\frac{2^{p_e}}{s_e} \geq T_c \alpha \beta c_\infty$. We finish the proof. \square

D.3 Proof of Lemma 3

Proof. We first expand the formula of \mathbf{m}_k :

$$\mathbf{m}_k = (1 - \beta_1) \mathbf{m}_{k-1} + \beta_1 \mathbf{g}_k = (1 - \beta_1)^2 \mathbf{m}_{k-2} + \beta_1 (\mathbf{g}_k + (1 - \beta_1) \mathbf{g}_{k-1}) = (1 - \beta_1)^{k-1} \mathbf{g}_0 + \beta_1 \sum_{t=1}^k (1 - \beta_1)^{k-t} \mathbf{g}_t.$$

Similarly, we also have:

$$\tilde{\mathbf{m}}_k = (1 - \beta_1)^{k-1} \mathbf{g}_0 + \beta_1 \sum_{t=1}^k (1 - \beta_1)^{k-t} \tilde{\mathbf{g}}_t.$$

Then, by Lemma 1, we have:

$$\bar{\mathbf{g}}_k = \mathbf{g}_k + \frac{1}{\beta} (\tilde{\mathbf{e}}_k - \tilde{\mathbf{e}}_{k+1}) + \hat{\mathbf{e}}_k - \tilde{\mathbf{e}}_k,$$

where we let $\mathbf{g}_k := \frac{1}{N} \sum_{n=1}^N \mathbf{g}_k^n$, $\tilde{\mathbf{e}}_k := \frac{1}{N} \sum_{n=1}^N \tilde{\mathbf{e}}_k^n$, $\hat{\mathbf{e}}_k := \frac{1}{N} \sum_{n=1}^N \mathcal{C}_d(\tilde{\mathbf{e}}_k^n)$. Then, we can get:

$$\sum_{i=1}^k \boldsymbol{\eta}_i \circ (\tilde{\mathbf{m}}_i - \mathbf{m}_i) = \frac{\beta_1}{\beta} \sum_{i=1}^k \boldsymbol{\eta}_i \circ \left(\sum_{t=1}^i (1 - \beta_1)^{i-t} (\tilde{\mathbf{e}}_t - \tilde{\mathbf{e}}_{t+1} + \beta \boldsymbol{\Delta}_t) \right),$$

where $\boldsymbol{\Delta}_t := \hat{\mathbf{e}}_t - \tilde{\mathbf{e}}_t$. Now, we element-wisely analyze the right side term to get its upper bound. For each element of the right side term (we omit the index of dimension to simplify the notation), we have:

$$\begin{aligned} & \left| \frac{\beta_1}{\beta} \sum_{i=1}^k \eta_i \left(\sum_{t=1}^i (1 - \beta_1)^{i-t} (\tilde{e}_t - \tilde{e}_{t+1} + \beta \Delta_t) \right) \right| \\ &= \left| \frac{\beta_1}{\beta} \sum_{i=1}^k \eta_i \sum_{t=1}^i (1 - \beta_1)^{i-t} (\tilde{e}_t - \tilde{e}_{t+1}) + \beta_1 \sum_{i=1}^k \sum_{t=1}^i \eta_i (1 - \beta_1)^{i-t} \Delta_t \right| \\ &\stackrel{\textcircled{1}}{\leq} \left| \frac{\beta_1}{\beta} \sum_{i=1}^k \eta_i \sum_{t=1}^i (1 - \beta_1)^{i-t} (\tilde{e}_t - \tilde{e}_{t+1}) \right| + \frac{\beta_1 \eta c_u}{2s_e} \sum_{i=1}^k \sum_{t=1}^i (1 - \beta_1)^{i-t} \\ &= \left| \frac{\beta_1}{\beta} \sum_{i=1}^k \eta_i \sum_{t=1}^i (1 - \beta_1)^{i-t} (\tilde{e}_t - \tilde{e}_{t+1}) \right| + \frac{\eta c_u}{2s_e} \left(k - \sum_{i=1}^k (1 - \beta_1)^i \right) \\ &\leq \left| \frac{\beta_1}{\beta} \sum_{i=1}^k \eta_i \sum_{t=1}^i (1 - \beta_1)^{i-t} (\tilde{e}_t - \tilde{e}_{t+1}) \right| + \frac{k \eta c_u}{2s_e}, \end{aligned}$$

where in ① we use the bound $|\tilde{e}_{k,i}^n| \leq T_c \alpha \beta c_\infty$ from the proof of Lemma 2, results from Lemma 5 and the assumption that $\frac{2^{p_e}}{s_e} \geq T_c \alpha \beta c_\infty$. Note that we have the following:

$$\begin{aligned}
& \left| \sum_{i=1}^k \eta_i \sum_{t=1}^i (1-\beta_1)^{i-t} (\tilde{e}_t - \tilde{e}_{t+1}) \right| \\
&= \left| \sum_{i=1}^k \left(\eta_i (1-\beta_1)^{i-1} \right) \tilde{e}_1 + \sum_{t=2}^k \left(\sum_{i=t}^k (\eta_i - \eta_{i-1}) (1-\beta_1)^{i-t} \right) \tilde{e}_t - \sum_{t=2}^k \left(\eta_k (1-\beta_1)^{k-t+1} \right) \tilde{e}_t \right| \\
&\stackrel{\textcircled{1}}{\leq} c_u \eta (T_c + 1) \alpha \beta c_\infty \sum_{i=1}^k \left((1-\beta_1)^{i-1} \right) + T_c \alpha \beta c_\infty \left| \sum_{t=2}^k \left(\sum_{i=t}^k (\eta_i - \eta_{i-1}) (1-\beta_1)^{i-t} \right) \right| \\
&\stackrel{\textcircled{2}}{\leq} c_u \eta (T_c + 1) \alpha c_\infty \frac{\beta}{\beta_1} + c_u \eta T_c \alpha \beta c_\infty \beta_1 (k-1),
\end{aligned}$$

where in ① we use the bound from Lemma 6, i.e., $e_1 \leq \alpha \beta c_\infty$ and $e_t \leq T_c \alpha \beta c_\infty$ for $t > 2$. In ②, we use the assumption $|\eta_i - \eta_{i-1}| \leq \beta_1 c_u \eta, \forall i \in [T]$.

Then, combining all bounds together, we can get the following:

$$\begin{aligned}
& \left| \frac{\beta_1}{\beta} \sum_{i=1}^k \eta_i \left(\sum_{t=1}^i (1-\beta_1)^{i-t} (\tilde{e}_t - \tilde{e}_{t+1} + \beta \Delta_t) \right) \right| \\
&\leq \left| \frac{\beta_1}{\beta} \sum_{i=1}^k \eta_i \sum_{t=1}^i (1-\beta_1)^{i-t} (\tilde{e}_t - \tilde{e}_{t+1}) \right| + \frac{k \eta c_u}{2 s_e} \\
&\leq \frac{\beta_1}{\beta} \left(c_u \eta (T_c + 1) \alpha c_\infty \frac{\beta}{\beta_1} + c_u \eta T_c \alpha \beta c_\infty \beta_1 (k-1) \right) + \frac{k \eta c_u}{2 s_e} \\
&\leq (T_c + 1 + \beta_1^2 k T_c) \alpha c_\infty c_u \eta + \frac{k \eta c_u}{2 s_e}.
\end{aligned}$$

Then, we can conclude that:

$$\mathbb{E} \left\| \sum_{i=0}^k \boldsymbol{\eta}_i \circ (\tilde{\mathbf{m}}_i - \mathbf{m}_i) \right\| \leq (T_c + 1 + \beta_1^2 k T_c) \sqrt{d} \alpha c_\infty c_u \eta + \frac{k \sqrt{d} \eta c_u}{2 s_e}.$$

We finish the proof. \square

D.4 Proof of Lemma 4

Proof. we denote $\mathbf{g}_k^{full} := \nabla f(\boldsymbol{\theta}_k)$ for convenience. Note that we have:

$$\begin{aligned}
\mathbf{m}_k - \mathbf{g}_k^{full} &= (1-\beta) \left(\mathbf{m}_{k-1} - \mathbf{g}_{k-1}^{full} \right) + (1-\beta) \mathbf{g}_{k-1}^{full} - \mathbf{g}_k^{full} + \beta \mathbf{g}_k \\
&= (1-\beta) \left(\mathbf{m}_{k-1} - \mathbf{g}_{k-1}^{full} \right) + (1-\beta) \left(\mathbf{g}_{k-1}^{full} - \mathbf{g}_k^{full} \right) + \beta \left(\mathbf{g}_k - \mathbf{g}_k^{full} \right).
\end{aligned}$$

Then, take expectation on both sides:

$$\begin{aligned}
& \mathbb{E} \left(\left\| \mathbf{m}_k - \mathbf{g}_k^{full} \right\|^2 \right) \\
&= (1-\beta)^2 \mathbb{E} \left(\left\| \mathbf{m}_{k-1} - \mathbf{g}_{k-1}^{full} \right\|^2 \right) + (1-\beta)^2 \mathbb{E} \left(\left\| \mathbf{g}_{k-1}^{full} - \mathbf{g}_k^{full} \right\|^2 \right) + \beta^2 \sigma^2 + \\
&\quad 2(1-\beta)^2 \mathbb{E} \left(\left\langle \mathbf{m}_{k-1} - \mathbf{g}_{k-1}^{full}, \mathbf{g}_{k-1}^{full} - \mathbf{g}_k^{full} \right\rangle \right) \\
&\leq \left((1-\beta)^2 + (1-\beta)^2 a \right) \mathbb{E} \left(\left\| \mathbf{m}_{k-1} - \mathbf{g}_{k-1}^{full} \right\|^2 \right) + \left(1 + \frac{1}{a} \right) (1-\beta)^2 \mathbb{E} \left(\left\| \mathbf{g}_{k-1}^{full} - \mathbf{g}_k^{full} \right\|^2 \right) + \beta^2 \sigma^2 \\
&\stackrel{\textcircled{1}}{\leq} (1-\beta) \mathbb{E} \left(\left\| \mathbf{m}_{k-1} - \mathbf{g}_{k-1}^{full} \right\|^2 \right) + \frac{(1-\beta)^2}{\beta} \mathbb{E} \left(\left\| \mathbf{g}_{k-1}^{full} - \mathbf{g}_k^{full} \right\|^2 \right) + \beta^2 \sigma^2 \\
&\leq (1-\beta) \mathbb{E} \left(\left\| \mathbf{m}_{k-1} - \mathbf{g}_{k-1}^{full} \right\|^2 \right) + \frac{(1-\beta)^2 L^2}{\beta} \mathbb{E} \left(\left\| \boldsymbol{\theta}_{k-1} - \boldsymbol{\theta}_k \right\|^2 \right) + \beta^2 \sigma^2,
\end{aligned}$$

where for ①, we set $a = \frac{\beta}{1-\beta}$. We finish the proof. \square